January 2015

PERFORMANCE EVALUATION OF AN AUTOMOTIVE THERMOELECTRIC GENERATOR

Andrei Olegovich Dubitsky
Purdue University

Graduate School Form 30
Updated 1/15/2015

PURDUE UNIVERSITY
GRADUATE SCHOOL
Thesis/Dissertation Acceptance

This is to certify that the thesis/dissertation prepared

By Andrei Olegovich Dubitsky

Entitled

PERFORMANCE EVALUATION OF AN AUTOMOTIVE THERMOELECTRIC GENERATOR

For the degree of Master of Science in Mechanical Engineering

Is approved by the final examining committee:

Stephen Heister
Co-chair

Xianfan Xu
Co-chair

Timothy Fisher

To the best of my knowledge and as understood by the student in the Thesis/Dissertation Agreement, Publication Delay, and Certification Disclaimer (Graduate School Form 32), this thesis/dissertation adheres to the provisions of Purdue University's "Policy of Integrity in Research" and the use of copyright material.

Approved by Major Professor(s): Stephen Heister, Xianfan Xu

Approved by: Ganesh Subbarayan 5/11/2015

Head of the Departmental Graduate Program Date

PERFORMANCE EVALUATION OF AN AUTOMOTIVE THERMOELECTRIC GENERATOR

A Thesis

Submitted to the Faculty

of

Purdue University

by

Andrei O. Dubitsky

In Partial Fulfillment of the

Requirements for the Degree

of

Master of Science in Mechanical Engineering

August 2015

Purdue University

West Lafayette, Indiana

ACKNOWLEDGEMENTS

I would like to begin by thanking the project sponsor Department of Energy for making this work possible. I would like to thank Professor Stephen Heister, Professor Xianfan Xu, Professor Timothy Fisher, Scott Meyer, and Rob McGuire for their time, guidance, support, and great patience. In particular I would like to thank Professor Heister and Professor Xu for giving me the opportunity to study and work at Purdue, and to this day I am amazed at how fortunate I am to count them as advisors. I would like to thank Sumeet Kumar for breaking the ground on this project and laying the foundations, and Shouyuan Huang for his help this past semester.

I have had the opportunity to work engineers at General Motors, Delphi, Dana, Marlow, and JPL who have been inspiring role models, and I would especially like to thank James Salvador and Mike Reynolds for their mentorship along the way.

Finally I would like to thank my parents for their support, advice, and encouragement through my time at Purdue.

TABLE OF CONTENTS

Page

Page

APPENDICES

LIST OF TABLES

Table Page

LIST OF FIGURES

Figure Page

Figure Page

NOMENCLATURE

Description	Symbol
Carbon nanotube	CNT
Cold Side Heat Exchanger	CHX
Corporate Average Fuel Economy	CAFE
Department of Energy	DOE
Environmental Protection Agency	EPA
Heating, Ventilation, Air Conditioning	HVAC
Hot Side Heat Exchanger	HHX
Internal Combustion Engine	ICE
Maximum Power Point	MPP
Maximum Power Point Tracking	MPPT
Piping and Instrumentation Diagram	P&ID
Radioisotope Thermoelectric Generators	RTG
Skutterudite	SKD
Solid State Relay	SSR
Thermal Interface Material	TIM
Thermoelectric	TE
Thermoelectric Generator	TEG
Thermoelectric Module	TEM

ABSTRACT

Dubitsky, Andrei O. M.S.M.E., Purdue University, August 2015. Performance Evaluation of an Automotive Thermoelectric Generator. Major Professors: Stephen Heister and Xianfan Xu, School of Mechanical Engineering.

Around 40% of the total fuel energy in typical internal combustion engines (ICEs) is rejected to the environment in the form of exhaust gas waste heat. Efficient recovery of this waste heat in automobiles can promise a fuel economy improvement of 5%. The thermal energy can be harvested through thermoelectric generators (TEGs) utilizing the Seebeck effect.

In the present work, a versatile test bench has been designed and built in order to simulate conditions found on test vehicles. This allows experimental performance evaluation and model validation of automotive thermoelectric generators. An electrically heated exhaust gas circuit and a circulator based coolant loop enable integrated system testing of hot and cold side heat exchangers, thermoelectric modules (TEMs), and thermal interface materials at various scales.

A transient thermal model of the coolant loop was created in order to design a system which can maintain constant coolant temperature under variable heat input. Additionally, as electrical heaters cannot match the transient response of an ICE, modelling was completed in order to design a relaxed exhaust flow and temperature

history utilizing the system thermal lag. This profile reduced required heating power and gas flow rates by over 50%

The test bench was used to evaluate a DOE/GM initial prototype automotive TEG and validate analytical performance models. The maximum electrical power generation was found to be 54 W with a thermal conversion efficiency of 1.8%. It has been found that thermal interface management is critical for achieving maximum system performance, with novel designs being considered for further improvement.

CHAPTER 1. INTRODUCTION

1.1 Introduction

Recent rapid increases in requirements for Corporate Average Fuel Economy (CAFE) are driving automotive manufacturers to explore many novel technologies for increasing vehicle efficiency. These standards are targeted to improve national energy security, save consumers cost at the pump, and reduce greenhouse gas emissions [1]. Transportation is a high impact area as it is the second largest energy use sector in the Unites States behind the industrial sector, as seen in Figure 1.1, and beginning in the new millennium passed the industrial sector to become the highest carbon dioxide emission source [2], as seen in Figure 1.2.

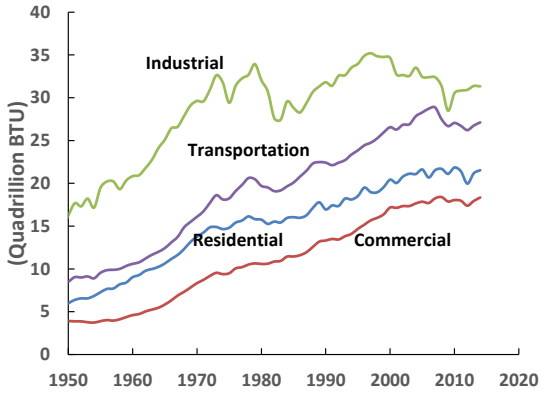

Figure 1.1: US Annual Energy Consumption by Sector [2].

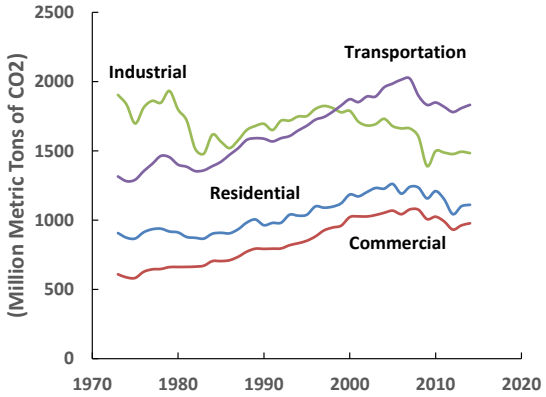

Figure 1.2: US Annual CO2 Emissions from Energy Consumption by Sector [2].

An ideal engine modelled by the Otto cycle with a compression ratio of 8 has a thermodynamic efficiency of 56%, leaving 44% of the primary fuel energy in the form of waste heat. A breakdown of energy utilization in a real engine based on literature and modelling results can be found in Figure 1.3, showing that about 65% of the fuel energy is rejected as waste heat, with the majority (35%) in the exhaust [3]. For a V-8 engine the exhaust gas thermal energy can vary from 50kW in heavy operation to 5kW at idle [4].

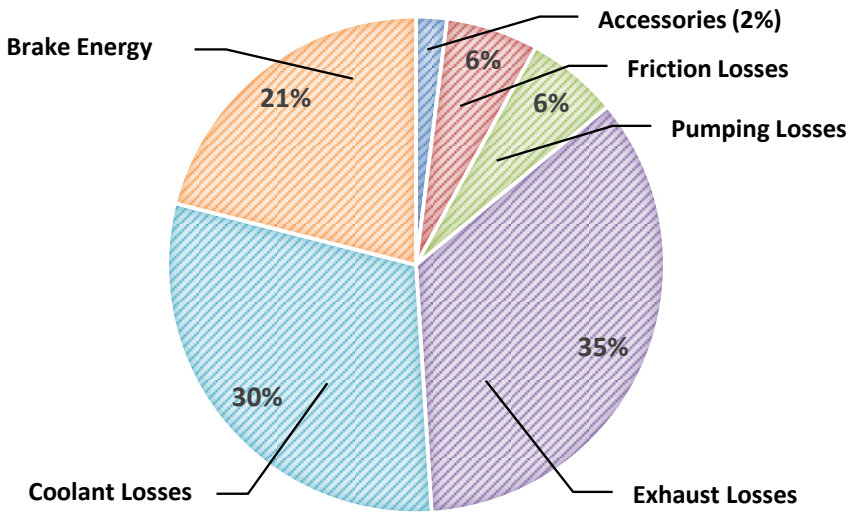

Figure 1.3: Energy Utilization on a US EPA City Driving Cycle for a Mid-Size Sedan [3].

A major challenge to attaining the theoretical engine efficiency is the wide range of operating conditions placed upon the engine, ranging from high torque and low rpm to low torque and high rpm. This prevents the engine from operating at an optimum state and further increases the energy lost as waste heat [5]. Further losses from the engine

output power include friction, coolant pumping losses, transmission losses, and braking losses [3].

Researchers are targeting every aspect of vehicle inefficiency for improvement. A selection of research areas includes low friction lubricants, increased compression ratios, mass reduction, drag reduction, turbocharging, cylinder deactivation, and waste heat recovery. Alternatives to traditional vehicles, such as hybrid and electric vehicles, are also being evaluated [5]. Overall the increasing efficiency standards are driving an exciting period in automotive innovation. This research focuses on the direct conversion of waste heat to usable electrical energy through the use of Thermoelectric (TE) Modules.

1.2 Thermoelectrics/Skutterudite (SKD)

Thermoelectric materials convert heat directly to electricity when a temperature gradient is applied to the junctions of dissimilar materials. This can be used to recapture some of the roughly 60% of produced energy in the United States which is wasted as heat [6]. Modeled by the Seebeck effect, thermoelectrics are widely and reliably used in thermocouples. Other thermoelectric applications include space vehicle power, vehicle waste heat recovery prototypes, solid state cooling, and temperature control [7].

Thermoelectrics have many attractive properties. They are solid state devices with no moving parts and can be silent and reliable, and by connection in series or parallel can be scaled for many footprints and electrical output characteristics [7]. There are, however, challenges to overcome for mass produced applications. Existing devices have lower conversion efficiencies than competing heat engine technologies. Automotive

applications have also uncovered concerns about reliability and durability, with deteriorating performance and failure resulting from thermal and mechanical stresses, oxidation, sublimation, and electrical degradation [7]. Commercialization obstacles include high cost and in some instances difficult to obtain, rare, or toxic raw materials.

A basic TE element can be seen in Figure 1.4 below, with critical components including hot and cold side heat exchangers, electrical insulators to prevent current leakage from the modules, electrical conductors to close the circuit between elements, diffusion barrier to isolate the thermoelectric materials, and the thermoelectric elements themselves [8].

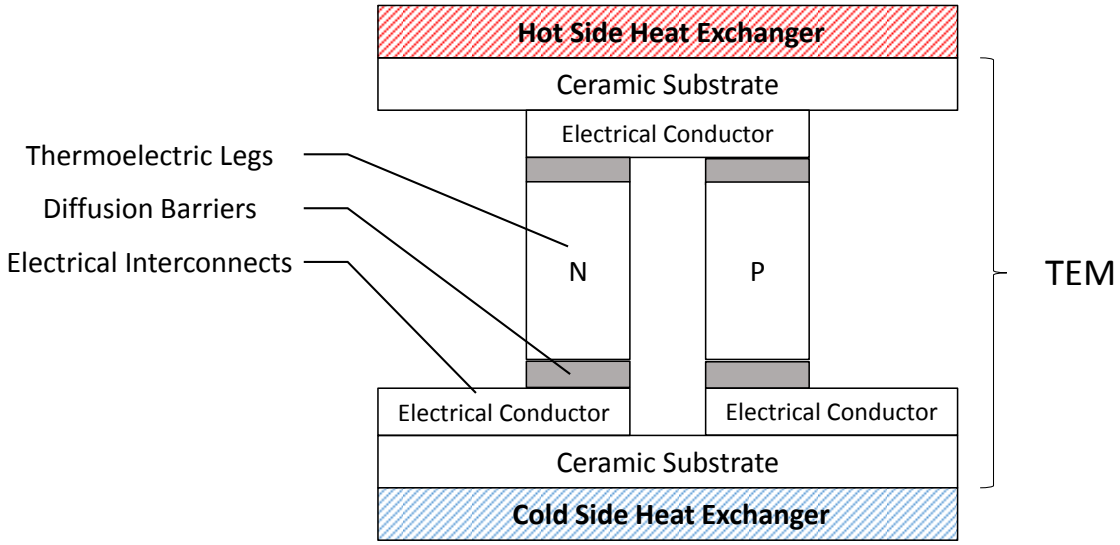

Figure 1.4: TE Module Schematic Diagram.

Thermoelectric materials are designed so that either electrons or holes, in 'n' and 'p' types respectively, act as mobile charge carriers, and generate an electrical potential under an applied temperature gradient. It is also important to consider the interfaces

between layers, which may have a significant impact on performance due to thermal and electrical contact resistance losses [9]. In order to protect the elements from oxidation and sublimation at high temperatures, modules may be contained in an inert environment, or otherwise coated to create a physical barrier [10].

The effectiveness of a thermoelectric material in converting thermal to electrical energy is represented as the figure of merit $ZT = \left(S^2 / \rho\kappa\right) \cdot T$, where S is the Seebeck Coefficient, ρ is electrical resistivity, and κ is thermal conductivity [4]. Values for popular thermoelectric materials are shown in the Figure 1.5.

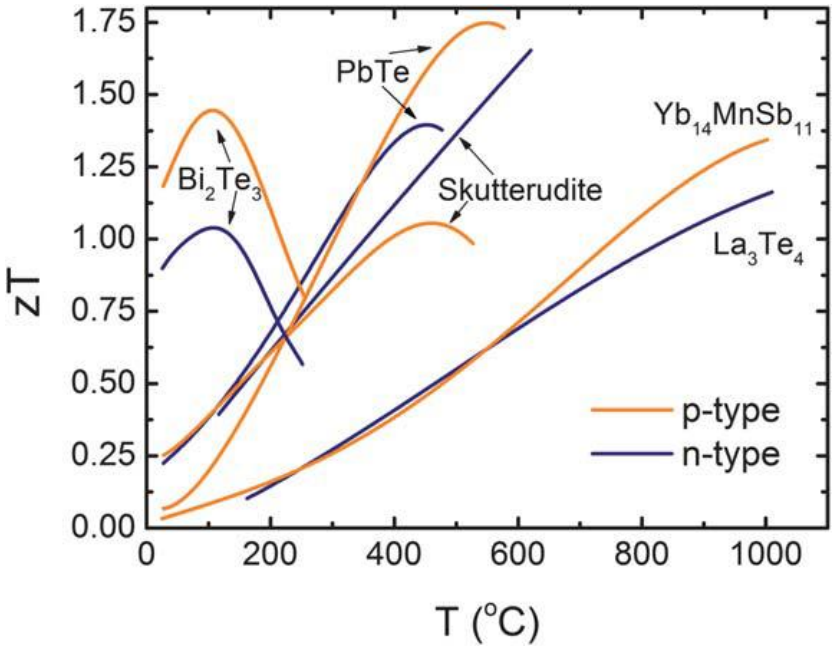

Figure 1.5: Thermoelectric 'n' and 'p' Type Figure of Merit [11].

While current materials have a ZT of around 1, advanced bench test materials have reported ZT values approaching 2 [11], with many promising results from nanomaterial

processing. Improvements in cost and performance of bulk materials and processing methods are driving factors in enabling mass produced thermoelectric applications [7].

In order to maximize efficiency and power generation, the temperature gradient across the thermoelectric modules must be maximized. In automobiles the hot exhaust downstream of the catalytic converter can exceed 675°C [4]. This temperature level can limit the effectiveness or restrict the use of some materials, such as Bismuth Telluride. Bismuth telluride is a common commercially available TEM found in applications including wine chillers, seat coolers, and camp stove power generators. A novel alternative TE material, Skutterudite (SKD), was tested in this research.

The conversion efficiency for a thermoelectric module is given in Equation (1.1) [4], where HM represents the hot side module temperature and CM the cold side module temperature, and $T_{avg} = 0.5\left(T_{HM} + T_{CM}\right)$.

$$\eta = \left(\frac{T_{HM} - T_{CM}}{T_{HM}}\right) \cdot \frac{\sqrt{1+ZT_{avg}} - 1}{\sqrt{1+ZT_{avg}} + \left(T_{CM} \big/ T_{HM}\right)} \tag{1.1}$$

Current overall converter efficiencies are low, typically around 5%, though future advances aspire to efficiencies upwards of 10% [12]. Efficiency advancements on the material side rely heavily on material science, in developing materials with high electrical conductivity and thermoelectric properties, while decreasing thermal conductivity to maximize the temperature gradient across the modules [13].

1.3 Thermoelectric Generators (TEGs)

Thermoelectric Generators (TEGs) are systems which employ numerous TEMs in order to generate electrical power. At a basic level, this requires four basic components. These are TEMs, hot side heat exchangers, cold side heat exchangers, and electrical conditioning for load compatibility [14]. TEGs have been used for numerous applications, including space, automotive, solar, remote sensing, industrial processes, power plants, electronics, and personal use. Currently numerous industrial and academic partnerships are developing TEGs for widespread applications [7].

Early TEGs utilizing nuclear decay as their heat source, known as radioisotope thermoelectric generators (RTGs), were launched in spacecraft in 1961. These devices have an exceptional track record of performance, with no failures in over 4 decades of use in over 26 space missions. The Voyager 1 and 2 missions launched in 1977 have been continuously operating on RTG power to the present day [15]. Several TEG units showing actual power generated are cataloged in Table 1.1.

Table 1.1: Summary of Notable TEG Systems.

System	Launch	Vehicle	Electrical Output
NASA Multi-Mission Radioisotope Thermoelectric Generator [15]	2011	Spacecraft	110 W
BSST DOE Automotive TEG [16]	2010	600° Test Bench	125 W
Clarkson Automotive TEG [17]	2005	1999 GM Sierra	150 W
GM Department of Energy Automotive TEG [18]	2012	Chevrolet Suburban	25 W

Table 1.1 includes automotive TEGs developed by Ford/BWM under BSST LLC and General Motors. It should be noted that vehicle applications present unique challenges compared to space applications due to the frequent thermal cycling, vibrations, and chemical environment [8]. Additional power is also required by the vehicle to transport the weight of the TEG, which decreases the net energy generation. A vehicle level layout showing the location and integration of TEGs is shown in Figure 1.6.

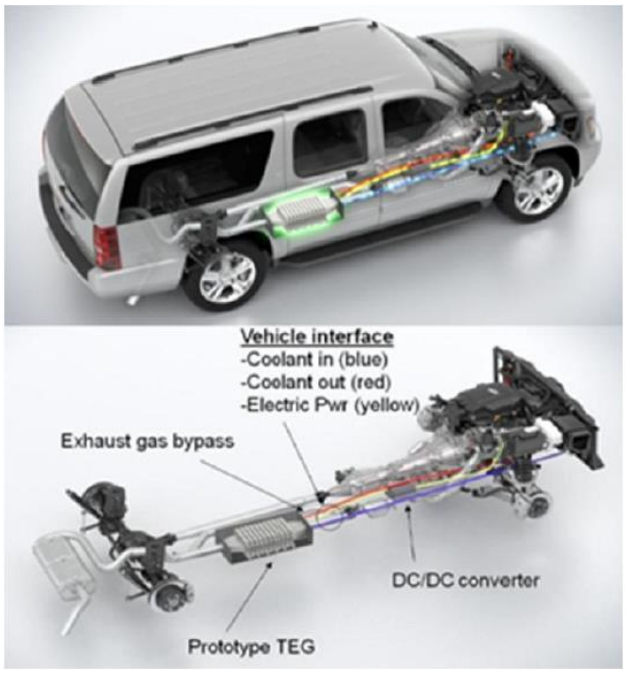

Figure 1.6: Vehicle Level TEG layout [18].

In automotive TEGs, the hot side heat exchanger interfaces with the exhaust gas and the cold side interface with the coolant. It is desirable to use the coolant as one of the thermal fluids due to its high heat transfer coefficients compared to gasses. Although it is possible to use the automotive coolant as the hot side fluid with ambient air on the

cold side, this results in a low ΔT of only about 100°C [18] and poor performance. Another important consideration is the pressure drop through the exhaust system, as additional backpressure may decrease engine performance [8]. TE material performance is reaching a point where the electrical power generated may exceed vehicle electrical needs, especially for most government fuel economy tests which limit accessory usage to approximately 350 W. This may be overcome by converting additional vehicle features to electrical operation, as well as application in hybrid vehicles which can utilize large amounts of generated power in the drivetrain [14]. Emerging technologies also utilize thermoelectrics for HVAC and battery thermal management applications [14].

A DOE sponsored project that the current work is based on developed and road tested an automotive TEG on a Chevrolet Suburban [18] shown in Figure 1.7. This system was the first of its kind to use Skutterudite (SKD) modules in a functioning prototype.

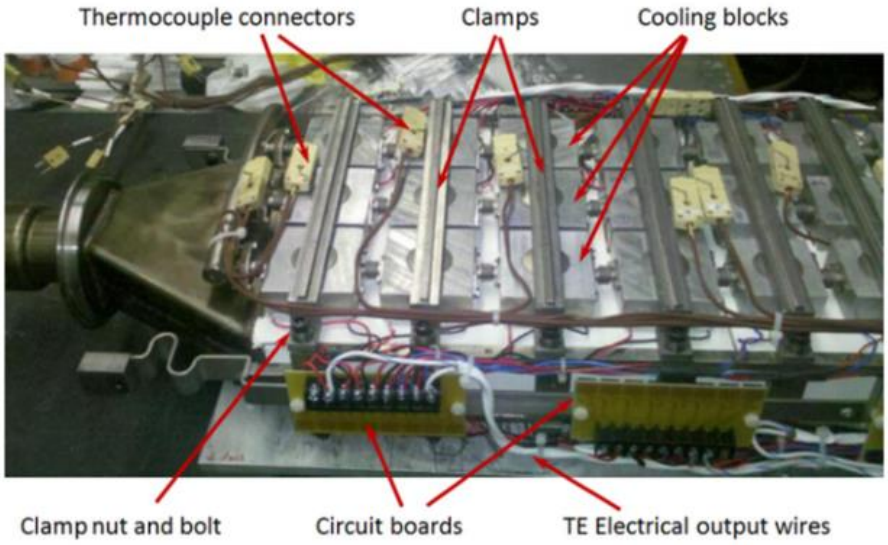

Figure 1.7: DOE Prototype Automotive Thermoelectric Generator [18].

SKD modules are desirable over Bismuth Telluride modules for their higher operating temperature. The design included both SKD and bismuth telluride modules, matching the optimum performance of each module to the temperature distribution of the TEG. The final configuration generated 25W of electrical power. The generator had to be run at lower temperature to protect the Bismuth Telluride modules, and it was estimated from module test stand results that under optimum temperature conditions the unit could generate 235 W. With improvements pursued in current research, mainly in the areas of thermal and electrical interfaces, it is predicted that the TEG could generate 425 W [18].

In order to maximize performance, current top performing TEG designs optimize thermoelectric materials with consideration of the heat sources and sinks [19]. In addition to the co-optimization of the electric and thermal impedance, the external electronic load can be varied to extract either maximum power through maximum power point tracking (MPPT) or maximum energy conversion efficiency. This has significant impact on the overall system performance. An additional area of optimization is the tradeoff between power output and material cost, which is critical to commercial applications as TE modules account for the majority of TEG cost [6]. A comprehensive approach to system design and optimization is necessary to produce the performance gains which may help thermoelectric use become feasible compared to many traditional power generation methods.

1.4 Numerical Modelling

A numerical model simulating coupled thermal and electrical physical processes in a TEG was developed at Purdue [9]. The model incorporates plate fin heat exchangers for the hot gas exhaust side and coolant cold side heat exchanger. Temperature dependent thermal and electrical properties are used for both SKD and bismuth telluride TE materials. A finite volume method is used to solve the domain in the fluid flow direction using thermal resistance networks along the heat flow path between the heat source and sink. The model outputs electrical power, heat transfer, and the system pressure drop [9].

This model was used for parametric evaluation and design optimization. With the goal of maximizing system efficiency, several topologies were considered, including rectangular configurations with either parallel or transverse flow, and radial configurations of circular and hexagonal heat exchangers, shown in Figure 1.8 [20].

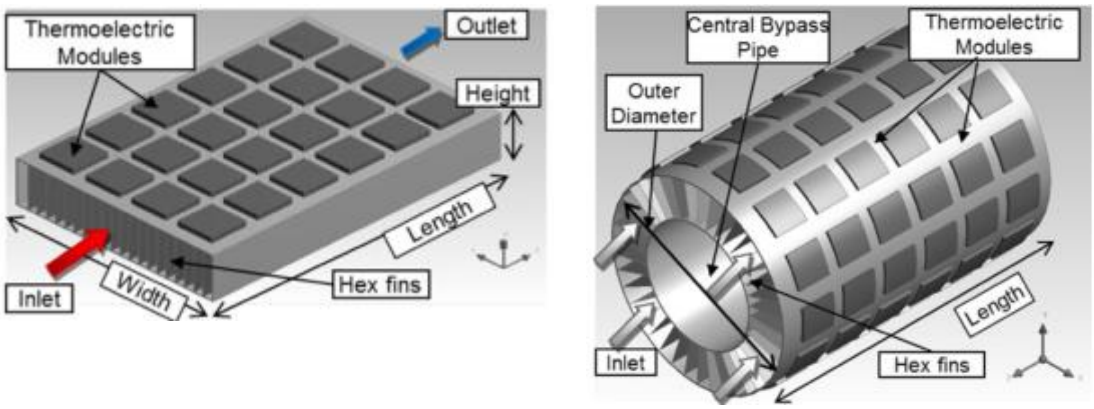

Figure 1.8: TEG Topologies Considered [20].

A typical design consequence of longitudinal heat exchangers is that the gas temperature drops along the length of the heat exchanger, reducing the available

temperature gradient to drive conversion. This prevents a single TEM design from covering the full range of temperatures within the TEG, as optimum TEM performance is achieved in a narrow band of conditions. Using multiple module types can allow more efficient operation, as considered in hybrid designs.

In each configuration the heat exchanger design, TEM arrangement, and TEG geometry was optimized [20], with design performance compared for a given volume constrained by the vehicle underbody geometry. The key findings were that heat exchanger fin enhancements could improve TEG power output by 30%, hybrid designs using multiple module types offered improved performance, and that the traverse flow configuration yielded the highest calculated power output of 730W. Additionally the optimized designs all performed near the allowable back pressure limit, suggesting that this is a limiting factor in TEG design [9].

1.5 Research Objective

The primary goal of this research was to develop a test rig capable of simulating vehicle exhaust gas and coolant in order to perform benchtop TEG performance testing in support of a Department of Energy (DOE) and General Motors R&D automotive thermoelectric project, “Development of Cost-Competitive Advanced Thermoelectric Generators for Direct Conversion of Vehicle Waste Heat into Useful Electrical Power”. The project is a broad collaboration between General Motors, Brookhaven National Labs, DANA thermal products, Delphi Electronics & Safety, Eberspaecher Exhaust Technology,

Jet Propulsion Laboratory, Marlow Industries, Michigan State University, Oak Ridge National Laboratory, University of Washington, and Purdue University.

Using exhaust gas and coolant streams on the test bench enabled full system testing, including multiple configurations of hot and cold side heat exchangers, TEMs, and thermal interface materials at various scales. Experimental data can be used to verify and correct analytical TEG models, evaluate generator performance, and optimize the system design. The test rig allows collection of early experimental data used to justify TEG design decision, and served as an intermediate step to engine dynamometer and demo vehicle testing.

CHAPTER 2. FACILITY DESCRIPTION

2.1 Overall Design

There are several levels of testing available for TEG performance evaluation, culminating in vehicle on board installation and road operation. This work focused on the development of a TEG test facility consisting of an electrically heated exhaust circuit and a coolant loop, shown in Figure 2.1.

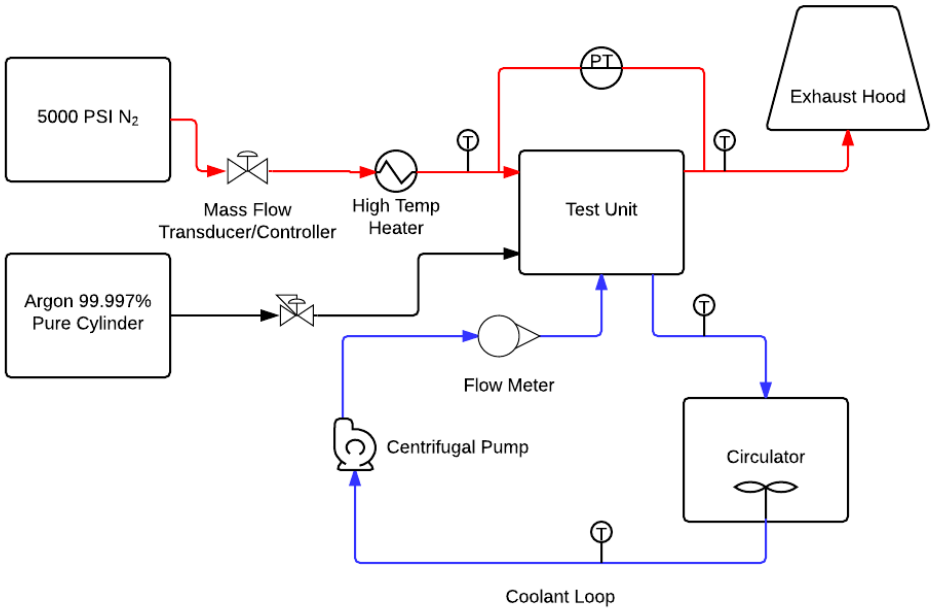

Figure 2.1: TEG Test Bench Diagram.

By providing well controlled inputs, removing additional complications of vehicle integration, and providing higher accessibility for measurements, bench testing allows early performance measurements and the opportunity for diagnosis and optimization of the TEG system. After passing bench testing, engine dynamometer testing is often used as it matches vehicle exhaust product composition, transient flow from the cylinders, and flow patterns [16].

There are several cycles used to standardize and simulate average driving behavior for the purpose of assessing vehicle performance. The US06 driving cycle was selected for benchmarking TEG performance [21]. This test cycle, shown in Figure 2.2, specifies vehicle speed as a function of time over a 596 second test covering a distance of 8.01 miles with an average speed of 48.37 mph. The speed varies from 0 to 80 mph throughout the test. The US06 is meant to simulate an aggressive high acceleration driving schedule.

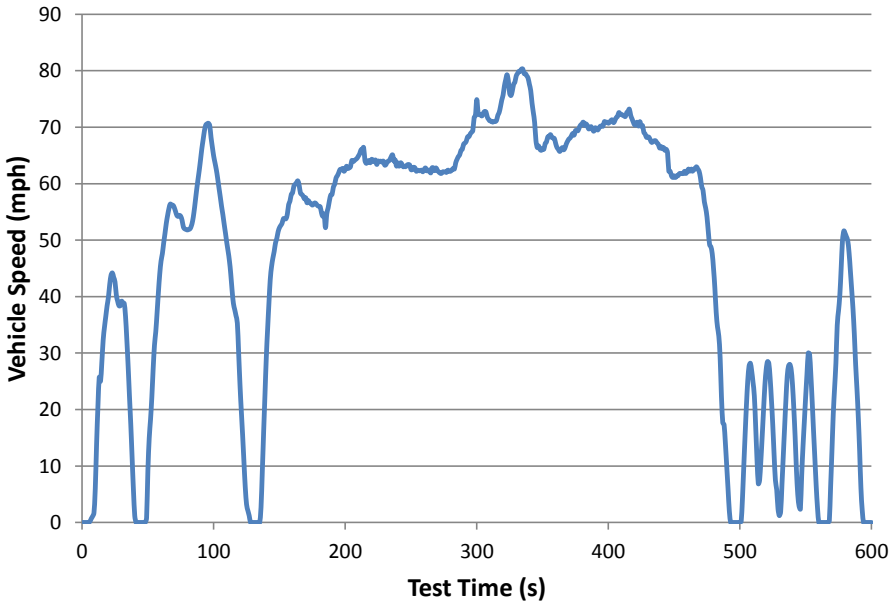

Figure 2.2: EPA US06 Driving Cycle [21].

This profile results in a highly transient exhaust flow rate and temperature history shown in Figure 2.3. The US06 cycle is performed after a warmup period that allows the coolant to reach steady state conditions, and thus the coolant flow rate and temperature is approximately constant.

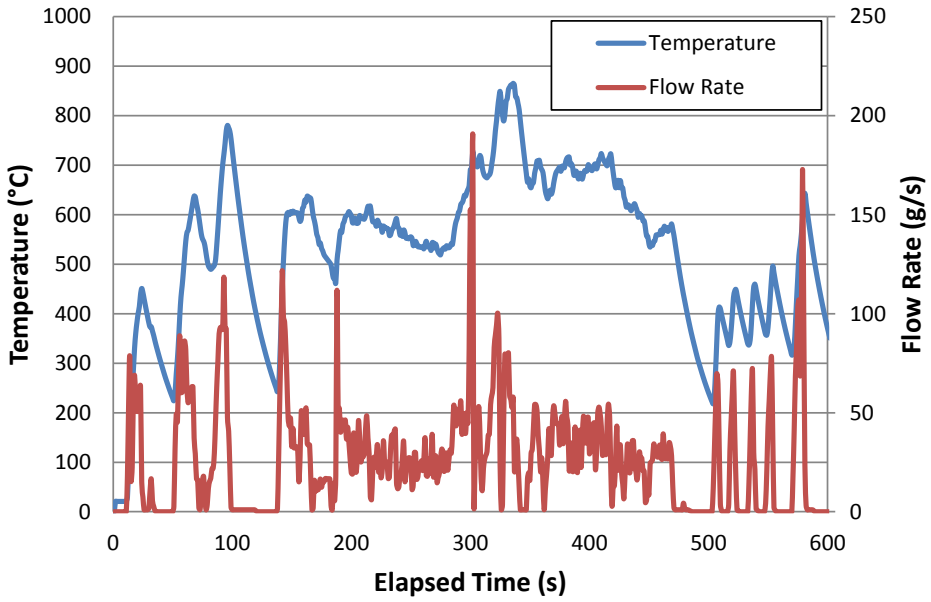

Figure 2.3: US06 Exhaust Temperature and Flow Profiles.

2.2 Exhaust Circuit Design

Both combustion and electrical heat sources were initially considered for simulating the exhaust gas in the test bench design. Using a combustion based heater had several advantages, including reaching higher temperatures, matching the chemical composition of the exhaust, and increased responsiveness for matching the rapid transients in the US06 cycle. A conceptual method was developed in order to allow varying both the

exhaust temperature and mass flow rate, shown in Figure 2.4. In this method, two separate streams would be used, a combustion gas stream and a dilution gas stream. The combustion gas stream would be composed of combustion air and fuel, burning at near complete combustion and giving a relatively fixed output temperature. By controlling the enthalpy input from this gas stream with cool air in the dilution stream, a variety of flow rates and temperatures may be achieved.

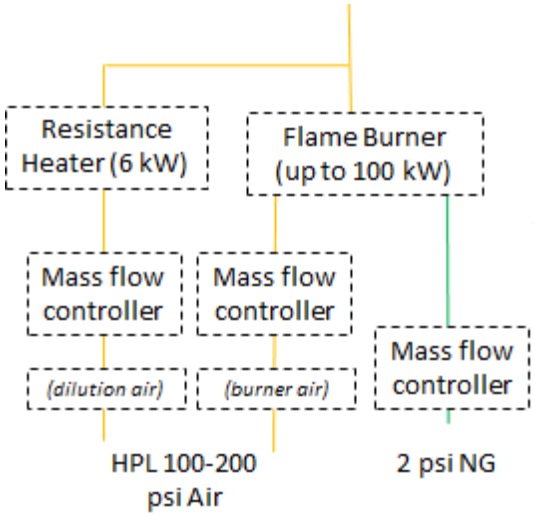

Figure 2.4: Conceptual Burner Layout.

Difficulties with this approach included finding a burner with a large turndown ratio and tolerance to high back pressure from the test unit. The electrical heater approach required a single gas stream with a variable electrical heater and power controller, and was selected on the basis of simplified control and scaling for different levels of testing. The electrical heater had a slower response time, however matching the exact US06 history was not required due to thermal lag in the system, which will be shown later.

For the bench testing, nitrogen was selected as the exhaust gas. The resulting inert environment was desirable for initial testing to protect the TEMs from oxidation in case of leakage. To check the fluid properties for similarity, nitrogen and exhaust gas were compared over the expected temperature range. The exhaust gas was approximated as complete stoichiometric combustion of octane. In reality gasoline is complex mixture of octane and other hydrocarbons and additives, and the combustion products include non-equilibrium and incomplete combustion products and particulates. Fluid properties were calculated for atmospheric pressure using reference equations of state from REFPROP [22]. A selection of the results appears in Table 2.1.

Table 2.1: Comparison of Exhaust and Test Bench Working Fluids.

Temperature [°C]	**200**	**300**	**400**	**500**	**600**	**700**	**800**
				Cp [kJ/kg-K]			
Nitrogen	1.053	1.070	1.092	1.116	1.140	1.162	1.182
Octane Complete	1.124	1.151	1.183	1.214	1.245	1.273	1.298
				Thermal conductivity [W/m-K]			
Nitrogen	0.037	0.043	0.049	0.054	0.059	0.064	0.069
Octane Complete	0.036	0.043	0.049	0.055	0.062	0.068	0.074
				Kinematic viscosity [cm^2/s]			
Nitrogen	0.349	0.483	0.633	0.797	0.976	1.168	1.372
Octane Complete	0.321	0.450	0.596	0.758	0.935	1.125	1.330

Thermal conductivity and Prandtl number were within 6% over the temperature range, while the specific heat and kinematic viscosity were within 10%. Heat exchanger fouling due to particulates and contact with non-inert species is also a concern in automotive applications, but is not evaluated in these tests.

Due to the highly transient nature of the US06 cycle, a heater can cover an acceptable range of cycle points without necessarily achieving the maximum required power. This is illustrated in Figure 2.5 below, which shows the distribution of heating power required to achieve US06 cycle points for a 1/10 scale test.

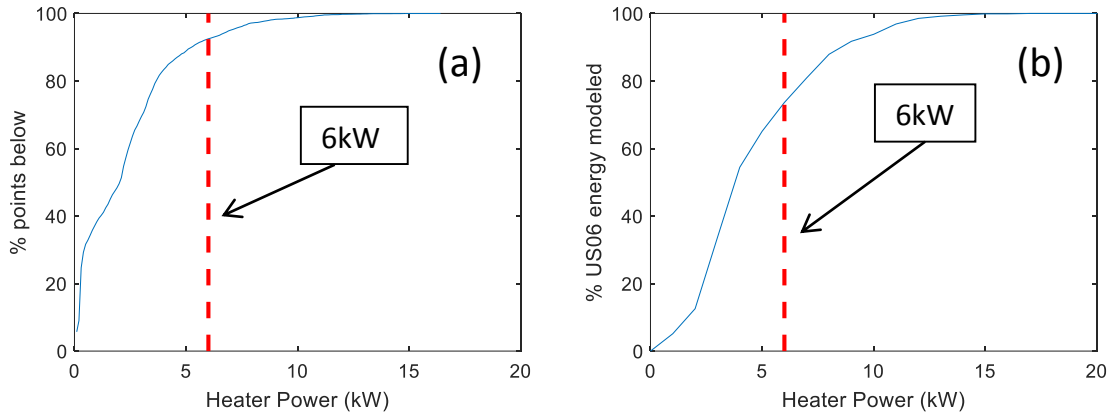

Figure 2.5: US06 Exhaust Power Distribution (a) and Modeled Energy Analysis (b).

Figure 2.5a shows the number of cycle points below a given exhaust power, while Figure 2.5b represents the percentage of the total exhaust energy in the cycle which could be covered. While a 13kW heater would be required to model the full cycle, a 6kW heater, which is significantly less expensive, covers 90% of the cycle points as seen in Figure 2.5a. and 70% the cycle energy shown in Figure 2.5b, as higher power points account for more energy. The main goal of the performance analysis is to assess the power generated by the TEG in order to calculate the fuel economy savings.

Due to limitations in the response time and capacity of the electrical heater and mass flow controller, it would be impossible to exactly recreate the cycle exhaust profile. Instead, a representative and achievable profile was created, which will be referred to as

the simplified US06 (US06S). The cycle was simplified by removing high frequency fluctuations which are attenuated due to the thermal mass of the TEG system. Candidate profiles were created using various filtering methods, including various length time filters and polynomial fitting, and compared with the actual US06 cycle using a transient thermal TEG model developed by Dana and JPL. A comparison of the TEM hot side temperature for the actual US06 cycle and US06S are shown in Figure 2.6 below for full scale, along with the reductions in heater and flow rate capacity resulting from smoothing the profile.

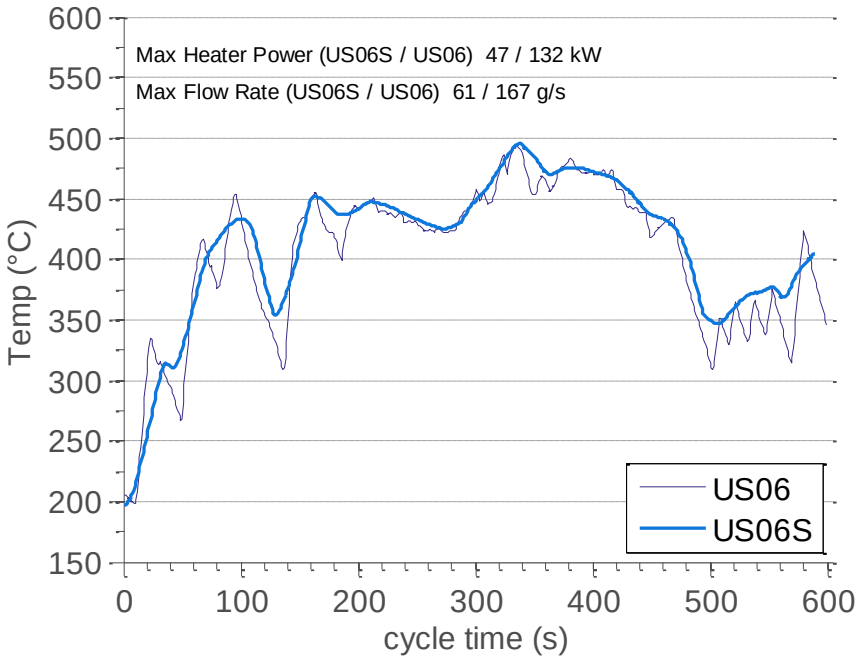

Figure 2.6: Hot Side TEM Leg Temperature for Simplified US06 Cycle.

It was assumed that the cold side temperature would be relatively constant, and in order to accurately match stress profiles and power generation, the hot side TEM temperature must be recreated.

A minimum heater power of 4.7kW was required to run the US06S profile at 1/10 scale. The heater selected was a Sylvania 038826 6kW Style B threaded inline air heater, which features an expected life of 5000 hours and a maximum outlet temperature of 760°C [23]. A Sylvania 057081 closed loop 25 A - 240 V phase angle fired power module was selected to control the heater power [23]. This was later upgraded to a Watlow open loop controller [24].

An Alicat MCR-250SLPM 250 SLMP flow controller [25] was used for controlling and measuring the gas flow rate up to 4.8 g/s of nitrogen. The mass flow controller has a settling time, defined as the time necessary to adjust to a new set point and settle to the controller's accuracy specifications, of 30ms. This feature was tested in recreating the exhaust mass flow rate profile by sending the controller new set points at a rate of 10Hz using serial communications from custom LabVIEW drivers, with the results appearing in Figure 2.7. The actual flowrate on average within 1 % of the desired flow rate.

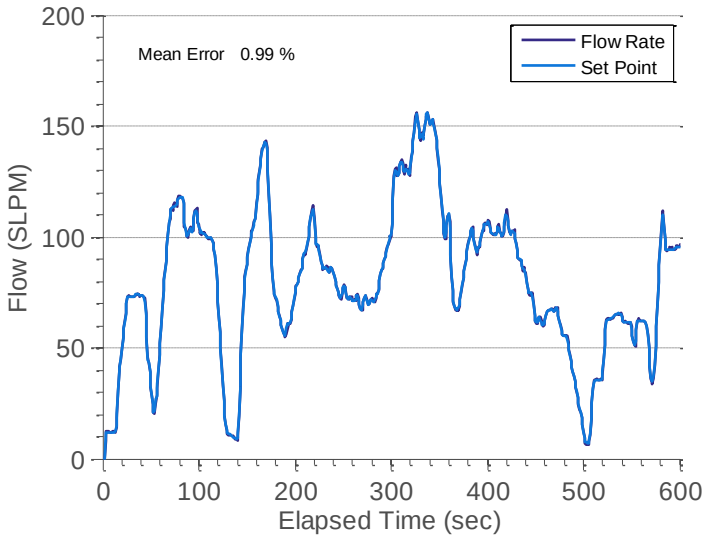

Figure 2.7: Flow Controller Transient Profile Tracking.

Engine back pressure is an important consideration for TEG system design. The differential pressure drop across the unit is measured with a Rosemount 3051C Pressure Transducer [26], which has a full scale range of 0-6000 Pa and an accuracy of +/- 10 Pa. The overall exhaust gas loop is shown in Figure 2.8.

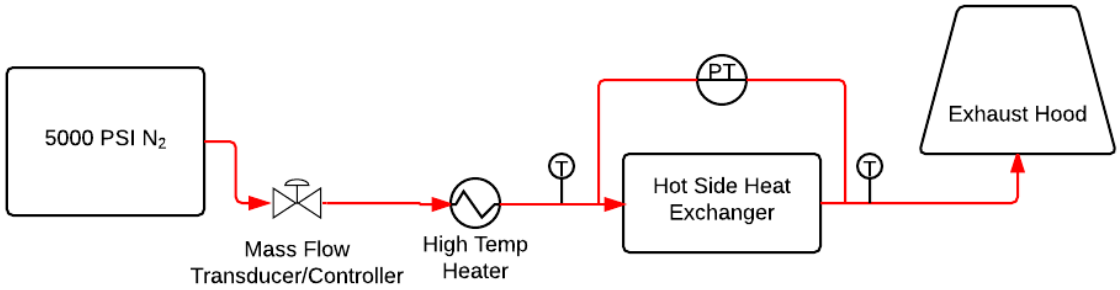

Figure 2.8: Exhaust Loop P&ID.

A larger scale exhaust test loop was also built, using an Alicat MCR-2000SLPM mass flow controller with a maximum flow rate of 38 g/s of nitrogen, and a Sylvania 074439 24kW Style B threaded inline air heater. The power was controlled using a Watlow # DC21-24S5-0000 Din-A-Mite SSR, which features an analog power modulation in 5% increments with variable time base zero-cross firing [24]. The Watlow SSR was controlled with a 0-10V analog output from the data acquisition system. This loop could be used for testing a larger 3/10 scale prototype TEG.

2.3 Coolant Loop Design

Coolant temperatures on a vehicle are nearly constant during normal operation in order to achieve maximum performance. The coolant loop must maintain a uniform coolant temperature while faced with widely varying heat loads, as well as limit maximum coolant temperatures in order to prevent boiling. A 50/50 mix of ethylene glycol based automotive coolant and distilled water is used in the coolant loop with inhibitors to prevent scale buildup and corrosion. The coolant loop P&ID is shown in Figure 2.9

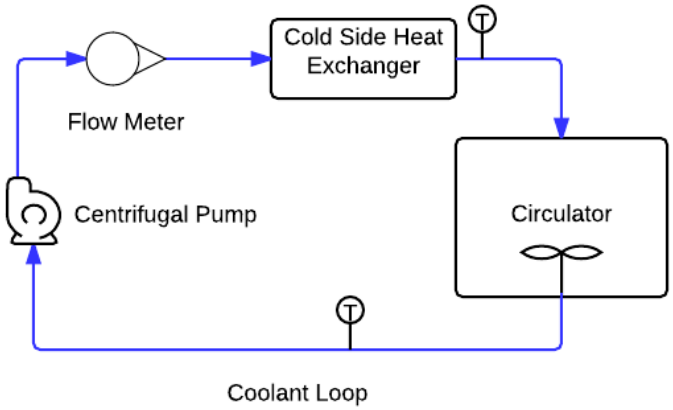

Figure 2.9: Coolant Loop P&ID.

On older automobiles the coolant temperature is effectively controlled using a mechanical thermostat valve, in which wax melts and expands at optimum temperatures opening a valve allowing coolant to flow to the radiator. In this application, a heated/refrigerated circulator was used to control the coolant temperature.

A transient numerical model was developed to estimate the coolant temperature throughout a US06 test. The model included heat input from the TEG, temperature control in the circulator, and fluid thermal storage, shown schematically in Figure 2.10.

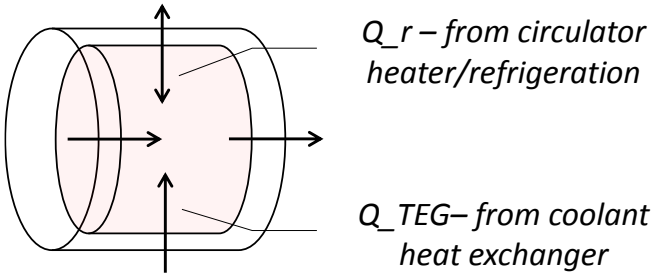

Figure 2.10: Fluid Energy Balance

The governing equation is 1D transient convection with a heating source term, in Equation (2.1). The fluid is treated as incompressible with constant properties in Equation (2.2), as little temperature change is expected. The finite volume method was used for discretization with a fully implicit scheme and 1st order upwind advection in Equation (2.3).

$$\frac{\partial}{\partial t}(\rho h)+\frac{\partial}{\partial x}(\rho u h)=S \tag{2.1}$$

$$dh=c_p dT \tag{2.2}$$

$$2T_n^t=0.5\left(T_{n-1}^t+T_n^{t-\Delta t}+{Q}/{\dot{m}c_p}\right) \tag{2.3}$$

Several additional assumptions were made in the model. The fluid was treated as plug flow, neglecting diffusion. The circulating bath reservoir was modeled as perfectly mixed with uniform temperature. The heat exchanger efficiency was assumed to be 60%.

The solution was found to be mesh independent for a 10x resolution increase. Additionally, the energy balance was checked by applying a heat input under otherwise adiabatic conditions and ensuring the final, well mixed coolant temperature had the expected temperature rise. For a heat input of 200kW a final temperature of 62.86°C was expected from the exact solution, while the model final temperature settled to 62.83°C.

The required cooling capacity is reduced in transient operation by utilizing the fluid as a thermal sink, as it can absorb a significant amount of energy with a minimal temperature rise. The model results showing fluid temperatures within the loop under a US06 transient input cycle are shown in Figure 2.11, where the reservoir temperature (TEG inlet temperature) is maintained at a nearly constant temperature as required.

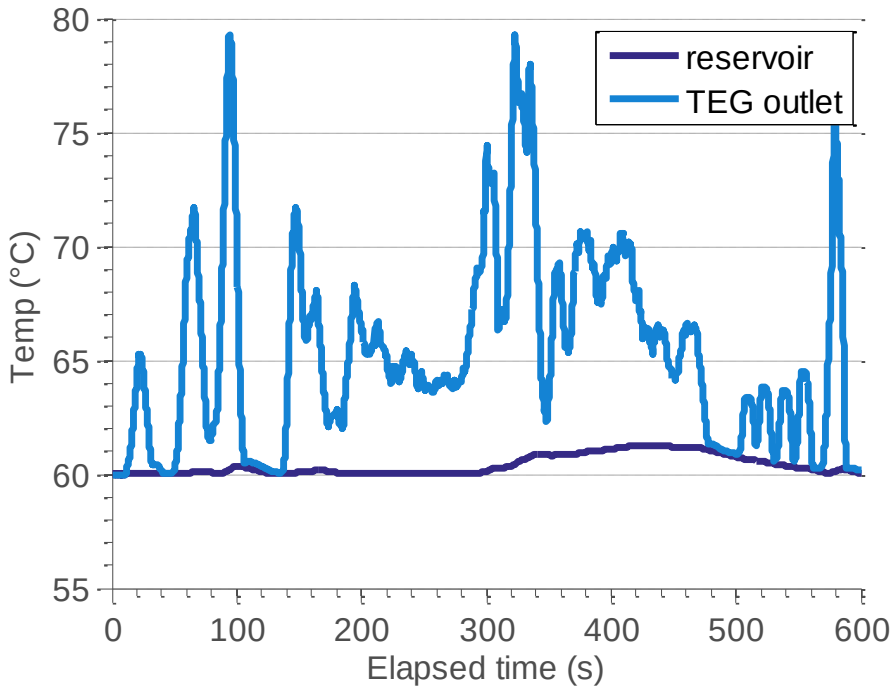

Figure 2.11: Coolant Loop Model Results.

Using results from this modelling, a 20L reservoir Polyscience MX20R-30-A11B circulating bath was selected, providing 1100 W of heating power, 915 W cooling at 20°C, and a maximum pump pressure of 1.8 psi [27]. Standard ½" radiator hose was used to make connections. It was found that the circulator pump alone could not achieve the desired flow rates, and an additional 8 psi magnetic drive pump (MARCH 815-BR [28]) was installed in series. The target flowrate was 3 L/min, and was measured using an OMEGA FL-9004 piston type variable area flow meter [29]. This model directly reads water flow rates and was adjusted for the automotive 50/50 ethylene glycol flow rate using a density effect correction factor given by $\sqrt{1.0 \,/\, \text{specific gravity}}$. At room temperature this gives a correction factor of 0.945. The viscosity correction factor is reported as negligible due to the use of a sharp edged orifice in the flow meter. The coolant loop arrangement showing the circulating bath, pump, flow meter, and tubing is shown in Figure 2.12.

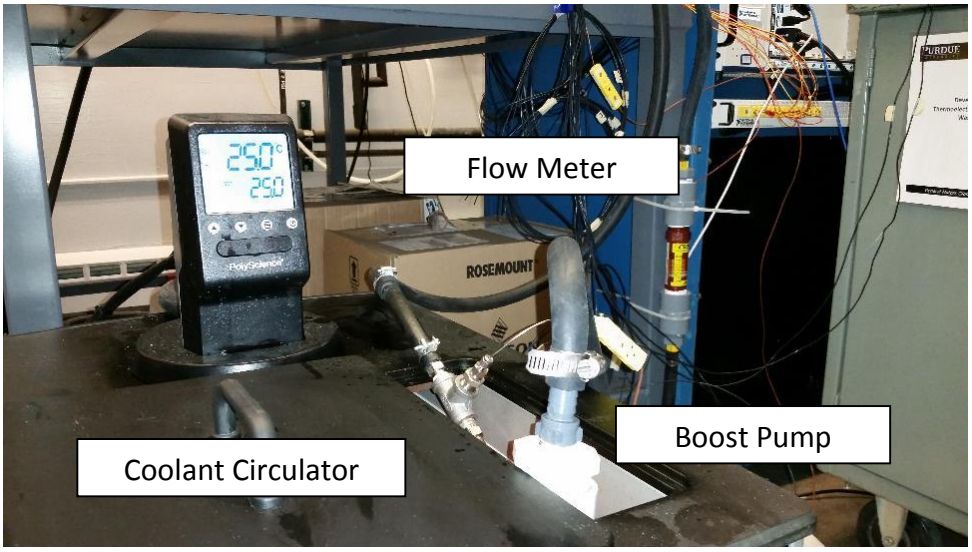

Figure 2.12: Coolant Loop Lab Setup.

2.4 Data Acquisition System Design

The data acquisition system is built on a LabVIEW PXI system, featuring integrated timing, synchronization, and a modular architecture allowing easy expansion for future applications. The system chassis is an NI PXIe-1078, 9-Slot 3U PXI Express, with a NI PXIe-8135 Core i7-3610QE 2.3 GHz Win 7 (64-bit) Controller. The analog input/output card is an NI-PXI 6255 [30], which has capacity for 80 analog voltage inputs or 40 differential inputs. It also has 24 digital I/O and 2 analog voltage outputs. All the inputs and outputs are connected using two SCB-68A Noise Rejecting, Shielded I/O terminal blocks with SHC68-68-EPM Shielded Cables. The thermocouple input module is an NI PXIe-4353 [31], which allows measurement of 32 thermocouple channels. The thermocouples connections are made on a NI TC-4353 Mini TC Terminal Block with a SH96-96-1 Shielded Cable. Both the data acquisition cards use one slot, leaving 6 card slots on the PXIe-1078 chassis open for future expansion. The channel capabilities are shown in Table 2.2.

Table 2.2: LabVIEW Measurement System Capabilities.

Measurement	**Channels**	**Resolution**	**Max Value**	**Min Value**
Analog Voltage Input	40 (diff.)	16 bit	-10 V	10 V
Analog Voltage Output	2	16 bit	-10 V	10 V
Digital I/O	24	x	x	x
Thermocouples	32	24 bit	-80 mV	80 mV

Based on an estimate of the thermal lag of the TEG, the system time constant was expected to be 0.1Hz. Using the recommended sampling rate of 10 times the maximum system frequency (based on the Nyquist theorem limit) predicts that a sampling rate of 1Hz would be sufficient to capture full system performance. The data acquisition system was conservatively developed using a 10Hz data acquisition rate.

At a full scale analog input of 10V, the system absolute accuracy is reported as 1920 μV, and the resolution is 153 μV. The analog input voltages are primarily used to measure the TEM output voltages up to 2.5 V per module. The thermocouple measurement accuracy has a maximum variability of 0.58°C for K type thermocouples between 300°C to 900°C at the upper range of the expected temperature range, and a variability of 0.38°C between 0°C and 300°C. The thermocouple measurement sensitivity for K type thermocouples is at most 0.11°C.

Using 32 thermocouple channels at 3 bytes/sample and 40 analog voltage inputs at 2 bytes/sample would result in a minimum required bandwidth of 1.76 kB/s. The total system bandwidth is 1 MB/s, so bandwidth was not a concern. Measurement synchronization was accomplished using a shared 10MHz sample clock and trigger. It was necessary to use separate measurement tasks in LabVIEW as the M-series PXI-6255 and X-series compatible PXIe-4353 devices do not support shared tasks. No pair of natively synchronized devices that supported the required channel counts was available.

Data is saved in the LabVIEW TDMS binary-based file format, which allows high speed data streaming and compact files, along with a built in hierarchy for documentation of data on file, group, and channel levels.

2.5 Power Conditioning System Design

Electronic loads are devices which can sink and measure current and voltage from power sources, operating as a variable resistor. An electronic load was selected in order to measure the high voltage and current produced by the TEG at various operating conditions for characterization of the TEG electrical performance. A BK Precision modular programmable DC electronic load was selected for this purpose. The system is built on one BKMDL001 mainframe, which can be configured to handle up to 2400 W of electrical power. The controller allows adjusting the load in constant current, constant voltage, constant resistance, and constant power modes. The unit has LAN, GPIB, USB, and RS-232 interfaces, with USB used for communication with the data acquisition system. The mainframe is expandable to double its available channels [32].

All four slots in the mainframe have BK Precision MDL400 Load modules. Each channel can sink 400 W of power at up to 80 V and 60 A. Thermoelectric modules have a low resistance and produce high current at relatively low voltages, which many electronic loads cannot handle. Both the current and voltage measurements are 16 bit, giving a voltage resolution of 1 mV up to 18V, and 10 mV up to 80V, and a current resolution of 0.1 mA up to 6 A, and 1 mA up to 60 A. The measurement accuracy is at least +/-(0.05% + 0.025% FS) for the voltage and +/-(0.05% + 0.05% FS) for the current. For TEG power measurements, this results in a resolution of 10mW with accuracy of ± (0.2 % + 0.2 % F.S.). The BK Precision Electronic Load has provided LabVIEW drivers which were used in order to interface the system with the data acquisition system for both read back and control.

2.5.1 Maximum Power Point Tracking (MPPT) Algorithm

Thermoelectric system power output depends on the operating conditions, specifically the hot side TEM leg temperature, the cold side TEM leg temperature, and the load electrical resistance. This relationship is often characterized with current/voltage (IV) curves, with the characteristic curves for example Skutterudite (SKD) TEMs used in and early TEG prototype shown in Figure 2.13. The strong temperature dependence of the current-voltage (IV) relationship is typical for thermoelectrics. IV sweep functionality is built into the LabVIEW data acquisition front end.

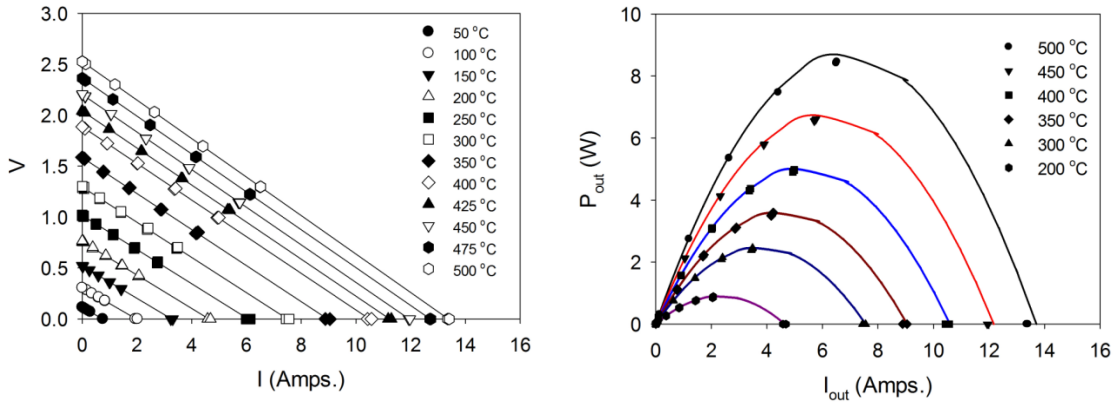

Figure 2.13: SKD Thermoelectric Module IV IP Curves as a Function of Temperature [4].

For any particular operating condition there is a unique point on the IV curve, known as the Maximum Power Point (MPP), which results in maximum power output from the TEG [33]. The location of this point is unknown, and must be found by employing Maximum Power Point Tracking (MPPT) in order to achieve maximum system efficiency.

MPPT algorithms have been classified as indirect methods, which use a database of performance curves to look up MPPs, and direct methods, which use measurements to track the MPP independently of known system characteristics [34]. Indirect methods were not considered as they are not as robust and require a large amount of memory.

There are many direct MPPT algorithms available, including Perturb/Observe methods (P&O), Incremental Conductance (IC), Current Sweep, and Open Voltage. In choosing a method, there are many practical considerations including simplicity, convergence speed, required hardware, cost, and performance [33]. The goal in this work was to estimate the ideal TEG performance, so the primary factor for selecting an MPPT algorithm was tracking ability.

The most basic MPPT method sets a constant operating voltage regardless of operating conditions. While easy to implement, this method has low efficiency. This can be improved by instead operating at a fixed percentage of the open circuit voltage, which can be shown to be roughly equal to the ideal MPP. This is the basis of the Open Voltage method, which periodically checks the system open circuit voltage and adjust the operating conditions based on the results [33]. The most direct MPPT method is to perform a full IV sweep at a given operating condition to find the exact MPP and continue running at that setting, however performing the sweep interrupts power generation and lowers efficiency.

Hill climbing methods determine their relative position on the Power-Voltage curve and incrementally step towards the MPP. These include P&O methods and IC methods. Perturb and Observe methods periodically make a small change to the voltage

or current and observe the resulting change in output power. If the power increases, the system may continue to make incremental changes in the same direction, otherwise it will move the operating point in the opposite direction [33]. P&O methods can suffer from oscillation and instability. There are many variations on P&O methods, notably ones which take several samples and dynamically adjust the step size [33].

An alternative hill climbing method is known as incremental conductance. This method is based on the fact that at the MPP the slope of the power-voltage curve is zero, and uses conductance measurements to determine the relative position of the MPP. This algorithm performs exceptionally well in rapidly varying environments and was selected for implementation for this project. This method can be further improved by using variable step sizes to both improve response speed and reduce steady state error [34].

Many MPPT algorithms are designed for use with inverters on power generating arrays, which have measurement latency at least an order or magnitude faster than electronic loads. As the current work uses an electronic load for testing, it was critical to minimize the number measurements to allow fast tracking, as well as select an algorithm adapted to electronic load operating modes [35]. A modified IC method for electronic loads (ICE) presented in Electronic Design [35] was used for this purpose. This method is designed to work specifically with the CV mode on electronic loads, with the flowchart shown in Figure 2.14.

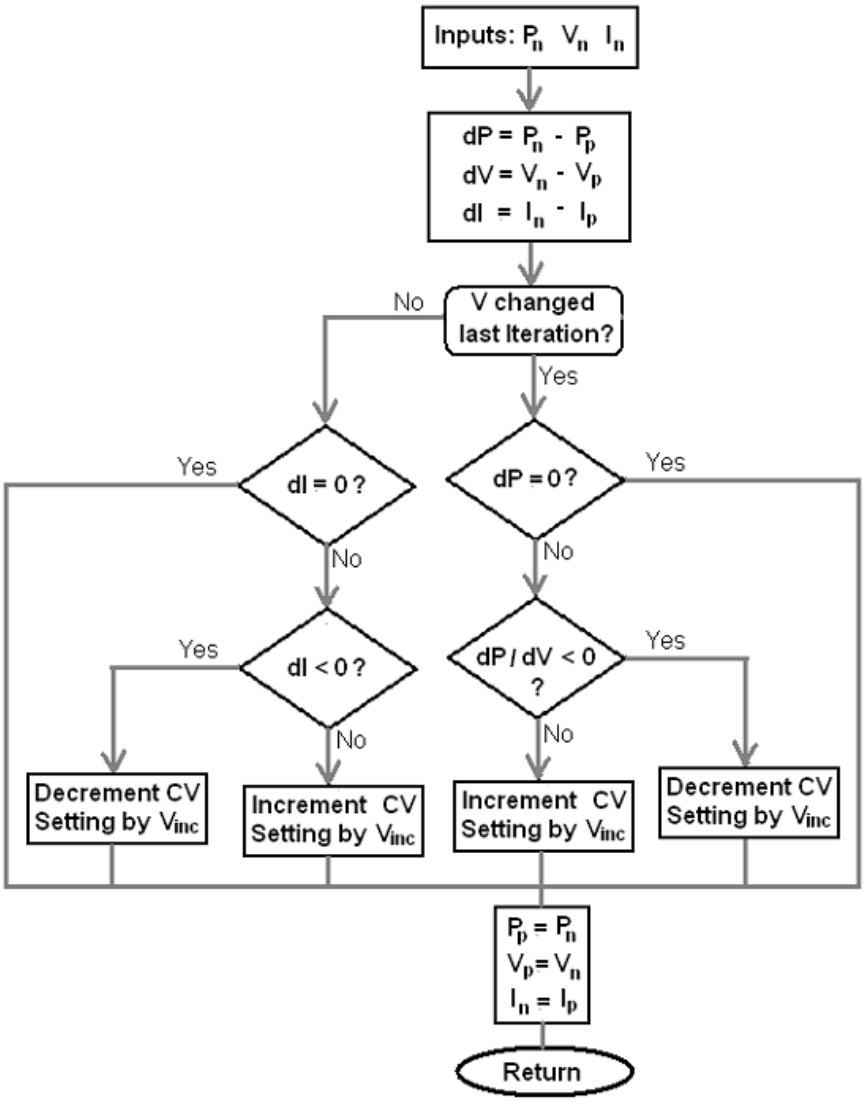

Figure 2.14: Modified Incremental Conductance MPPT for Electronic Loads [35].

2.5.2 Maximum Power Point Tracking (MPPT) Results

The ICE MPPT algorithm was implemented in the LabVIEW data acquisition front end. A step size of 20mV was used with an update rate of 1Hz. The tracking performance was tested by comparing the achieved MPP to results from steady state IV curves, taken sequentially at identical conditions to minimize complicating factors. The tracking results are shown in Figure 2.15. It was found that the algorithm converged to within 5% of the actual MPP. Note that in actual operation the TEG will begin from a steady state condition before transient profiles are applied, so the initial MPPT tracking from 0 mV will not impact the power output.

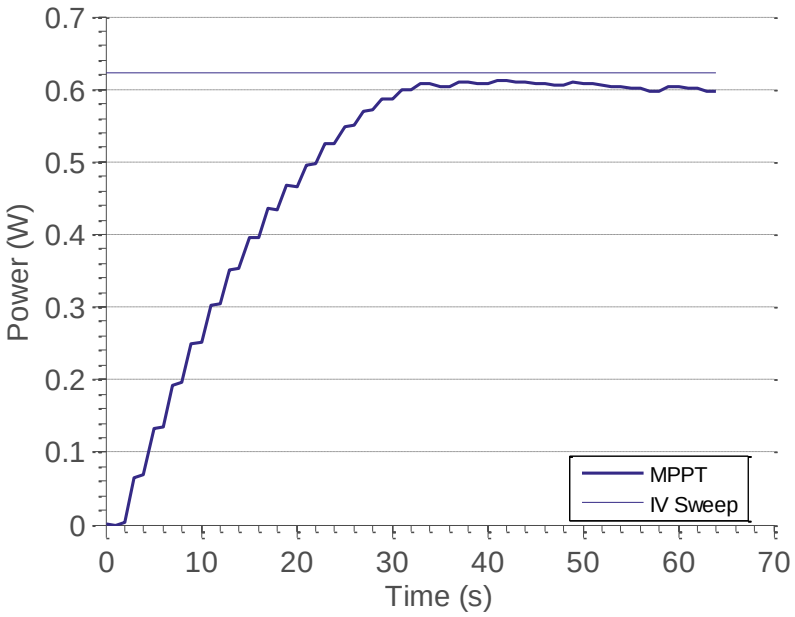

Figure 2.15: MPPT Tracking Results.

2.6 Summary

A test bench consisting of an electrically heated exhaust loop and a circulator based coolant loop was developed, and is shown in Figure 2.16.

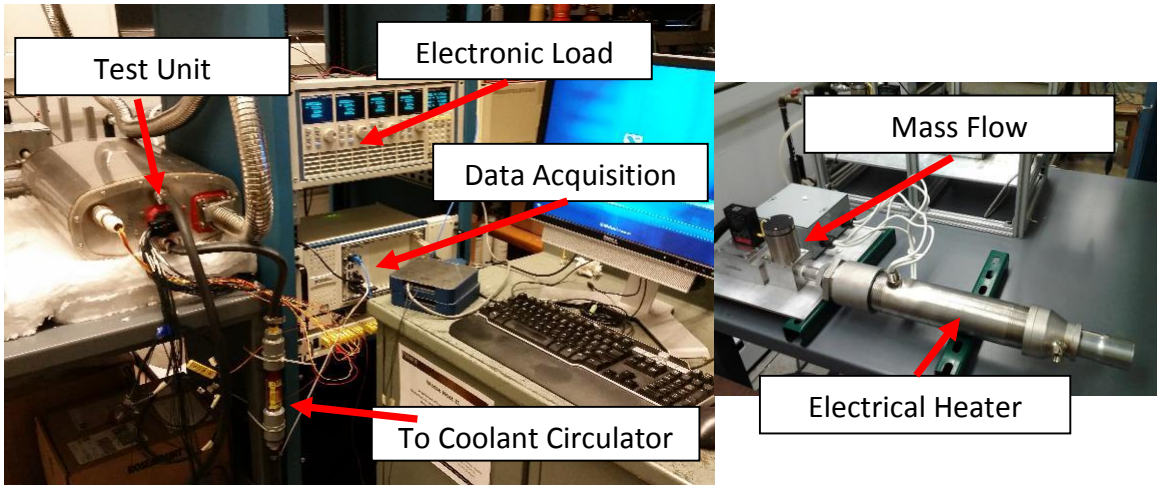

Figure 2.16: Test Bench Photos.

The test bench consists of an electrically heated exhaust circuit that can run at either 6kW heating 4 g/s nitrogen or 24kW heating 40 g/s nitrogen up to gas temperatures of 750°C, a circulator based coolant loop that can operate between 0°C and 90°C, a data acquisition system with 40 analog input voltages and 32 thermocouple channels, and an electronic load with 4 channels at up to 80V and 60A each. The LabVIEW front end allows monitoring flow rate, unit temperatures, individual TEM performance, overall TEG power output, and pressure drop under various exhaust flow rate and temperature profiles.

CHAPTER 3. TEG DESCRIPTION AND TEST RESULTS

3.1 Thermoelectric Generator (TEG) Layout

A TEG was designed as a collaborative effort between General Motors, Brookhaven National Laboratory, DANA thermal products, Delphi Electronics & Safety, Eberspaecher Exhaust Technology, Jet Propulsion Laboratory, Marlow Industries, Magnequench Inc., Michigan State University, Oak Ridge National Laboratory, University of Washington, and Purdue. The full on-vehicle TEG would consist of 10 "subassemblies" split between two TEG "subunits", due to space constraints on the test vehicle. A single TEG subassembly (1/10 scale) shown in Figure 3.1 was built for performance evaluation.

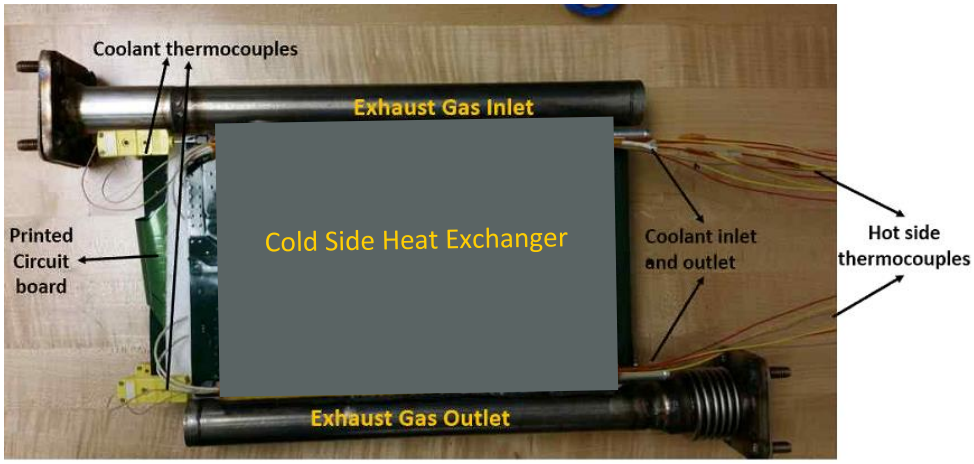

Figure 3.1: TEG Layout (Top View).

The unit was built around a single stainless steel hot side heat exchanger (HHX) located between two aluminum cold side heat exchangers (CHX). Skutterudite TEM modules were positioned between the HHX and CHXs using a printed circuit board, which also routed power and signal lines out of the TEG. The HHX was welded onto a slot machined into the sides of the inlet and outlet pipes. These features can be seen in the side view in Figure 3.2

Clamping was achieved using threaded rods and nuts (see Figure 3.2). The thermal interface between the module and the HHX was graphite foil, and the cold side thermal interface was a Honeywell thermal paste. The entire assembly was contained within a stainless steel case, which was purged and filled with argon gas maintained at a gauge pressure of 5 psi in order to protect the TEMs from oxidation.

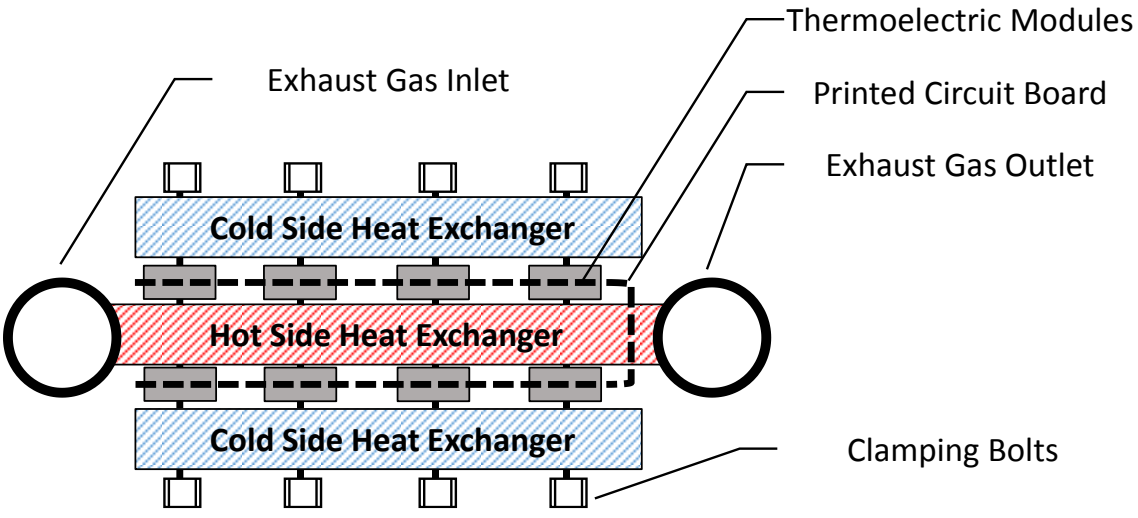

Figure 3.2: TEG Layout (Side View).

The TEMs were arranged in 4 rows with row 1 at the HHX inlet and row 4 at the HHX outlet. Each row consisted of 8 series connected TEMs, shown in Figure 3.3. Each row of modules on the circuit board was folded around the hot side heat exchanger, with 4 modules located on top surface of the HHX and 4 modules on the bottom surface of the HHX. The goal of this design was to have all modules within a row operating at similar voltages to minimize electrical losses. This would be facilitated by the expected uniform heat exchanger surface temperatures across each row of modules.

Two different module designs were used in the TEG, Type 1 modules were used for the first 3 rows, and smaller Type 2 modules were used for the last row on the trailing edge of the heat exchanger. The Type 2 modules were optimized for operation at lower hot side temperatures.

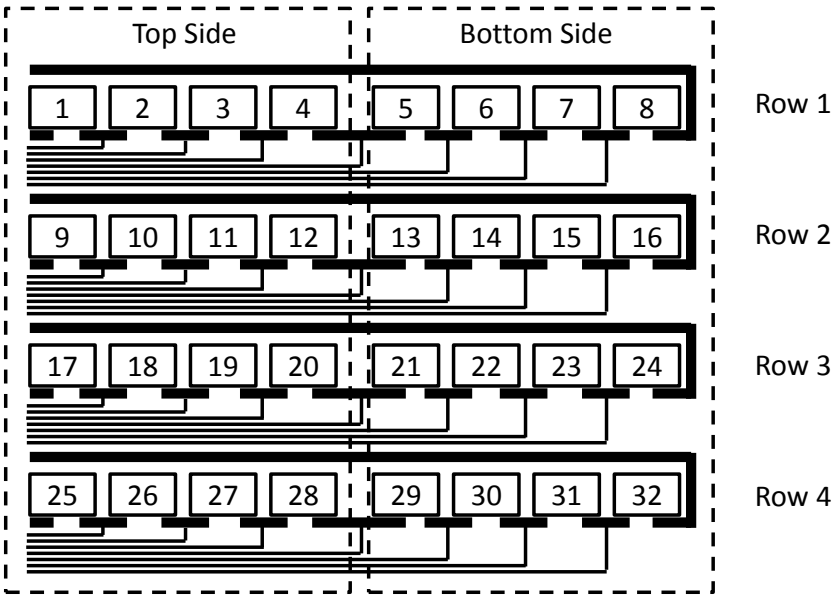

Figure 3.3: TEM Circuit Board Layout.

A full channel list is shown in Table 3.1. There are 5 coolant thermocouples, located in the inlet and outlet of the two cold side heat exchangers, and in the combined coolant outlet. These allow evaluation of heat rejection rates to the coolant as well as ensuring the maximum operating temperature is not exceeded.

Table 3.1: System Channel List.

1 Sub Assembly (1 HHX, 2 CHX, 1 PCB, 32 TEM)

# Channels	Location / Type	I/O	Lower	Upper	Unit	System
	TEMPERATURE MEASUREMENTS					
4	Coolant Heat Exchanger (CHX) Inlet/Outlet Temp TC, x2 CHX	I	0	150	°C	NI PXI
8	Hot Heat Exchanger (HHX) TC	I	0	800	°C	NI PXI
2	HHX Inlet/Outlet TC	I	0	800	°C	NI PXI
1	Heater Outlet Temp	I	0	800	°C	NI PXI
2	Coolant Circulator Inlet/Outlet Line Temp	I	0	150	°C	NI PXI
1	Mass Flow Controller Inlet Temp	I	0	50	°C	Alicat
	TEM MEASUREMENTS					
24	Individual TEM Voltage Sense Measurements	I	0	10	VDC	NI PXI
4	TEM Row VoltageMeasurements	I	0	10	VDC	BK EL
4	TEM Row Current Measurements	I	0	40	ADC	BK EL
	EXHAUST AND COOLANT CONTROL					
1	Coolant Flow Rate (EGW)	I	0	20	LPM	meter
1	Electrical Temperature Set Point Control	O	0	800	°C	NI PXI
1	Gas Flowrate	I	0	250/2000	SLPM	Alicat
1	Gas Setpoint	O	0	250/2000	SLPM	Alicat
	Pressure Drop					
1	Differential Pressure	I	0	6000	Pa	3051C
1	Mass Flow Controller Inlet Pressure	I	0	150	psi	Alicat

The exhaust temperature is monitored with thermocouples on the inlet and outlet of the TEG inserted perpendicular to the flow and located in the pipe centerline. In addition to this, 6 thermocouples are bonded to the hot side heat exchangers in locations shown in Figure 3.4. These thermocouple allow measurement of the hot side heat exchanger skin temperatures. One thermocouple was freely located in the TEG case to monitor the interior argon gas temperature. A final thermocouple was attached to the printed circuit board to ensure that it stayed within a safe operating temperature range despite its close proximity to the hot side heat exchanger.

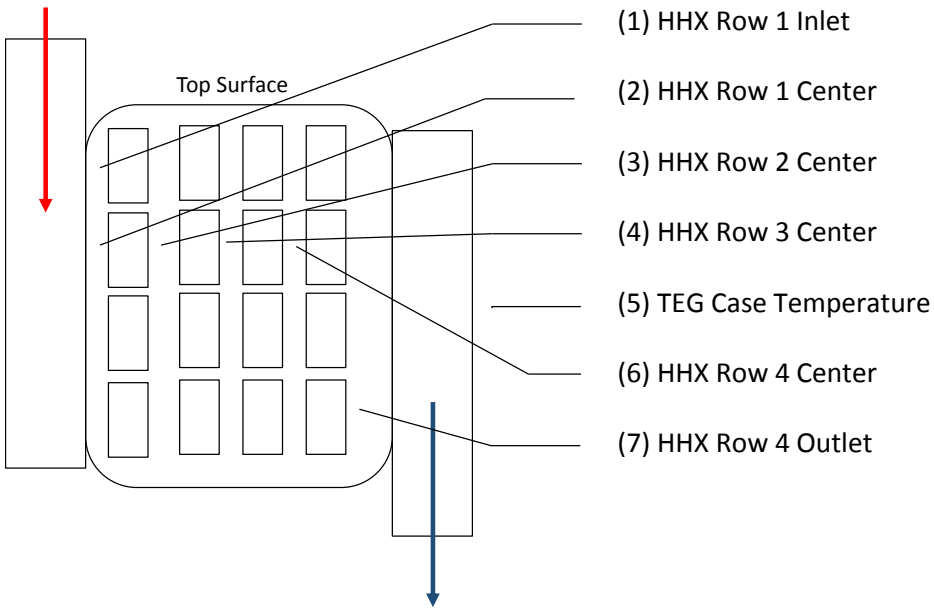

Figure 3.4: Hot Side Heat Exchanger Thermocouple Locations.

3.2 Testing

3.2.1 Thermal Performance

Initial testing of the GM/DOE TEG 1/10 scale TEG was completed using the developed test bench. The first testing goal was to ensure basic functionality at operating temperatures. To this end a slow temperature ramp was applied in stages, checking for TEM performance degradation before increasing exhaust temperatures.

A hot side temperature history for warm-up to the maximum design heat exchanger skin temperature of 500°C is shown in Figure 3.5. At this condition there was a HHX skin temperature drop of 235°C and a gas flow temperature drop of 460°C from inlet to outlet. These result indicate a bypass will be required for higher exhaust temperatures. The exhaust flowrate was 3.3 g/s, increasing to 3.6 g/s at 105 min and 4.0 g/s at 145 min.

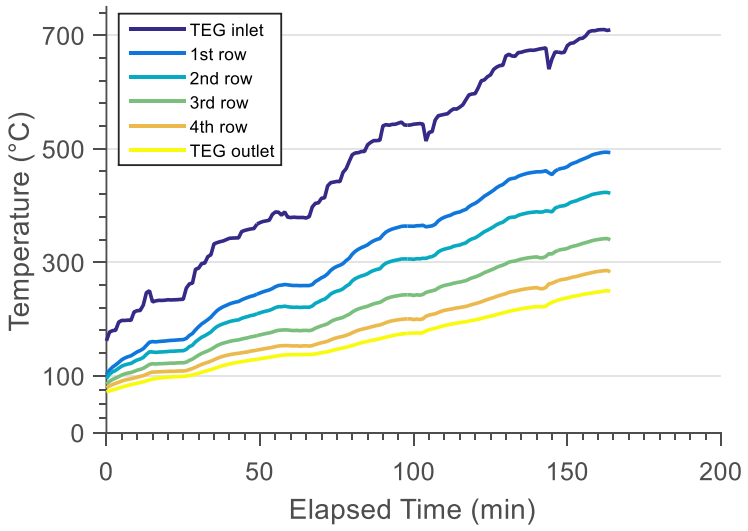

Figure 3.5: TEG Heat-up Hot Side Temperature History.

The coolant temperature history is shown in Figure 3.6. The coolant flow rate was 3.1 LPM. Temperature measurements were taken at the inlet and outlet of both cold side heat exchangers, and in the combined return line to the circulator.

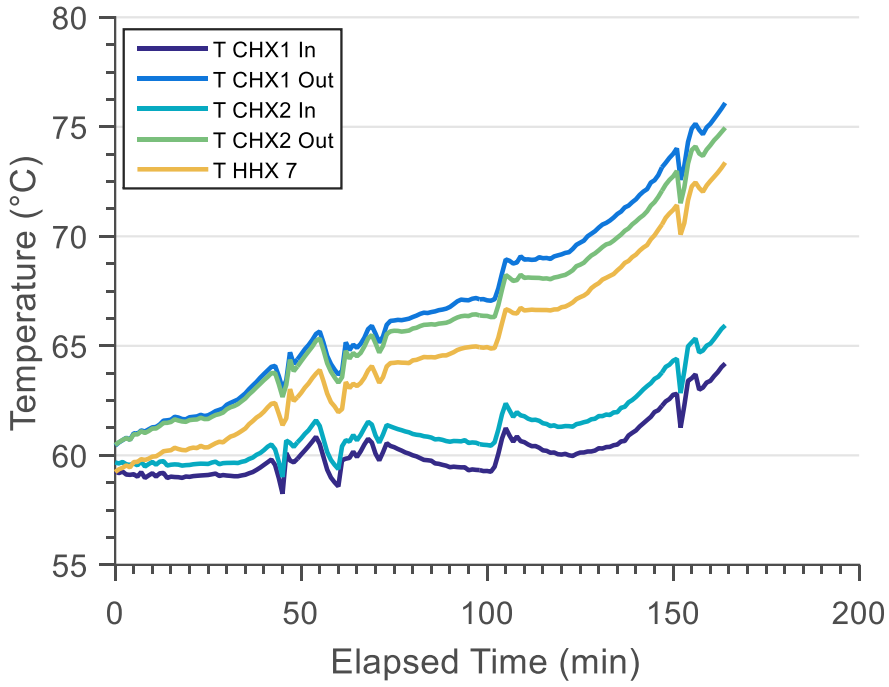

Figure 3.6: TEG Heat-up Coolant Temperature History.

The circulator was not able to maintain a constant coolant temperature over the extended test time, and under increasing heat loads from the heat exchanger experienced an inlet temperature increase of 5°C at the tested design point. There was a larger coolant temperature increase across CHX 1 than CHX 2, while similar TEM performance on the top and bottom sides of the hot side heat exchanger suggests that both CHXs experience similar heat flux. This could indicate a higher coolant flow rate though CHX2 and possible minor restriction in CHX1.

The slow heat-up data was used to verify the numerical coolant loop model described previously, with results shown in Figure 3.7. The cooling capacity of the chiller was increased from 1kW to 1.5kW to adjust for heat losses from the tubing connections, and also for the increased performance of the refrigeration loop for higher fluid temperatures. The model correctly predicts the point where the loop cooling capacity is exceeded by the heat input, and matches the excess temperature in the fluid. These results suggest that the model is accurately describing the system, and increases confidence in the prediction that the coolant loop will maintain constant temperatures over short transient cycle testing as designed. Note that the model does not account for thermal storage in the TEG, resulting in the initial deviation from the experimental results.

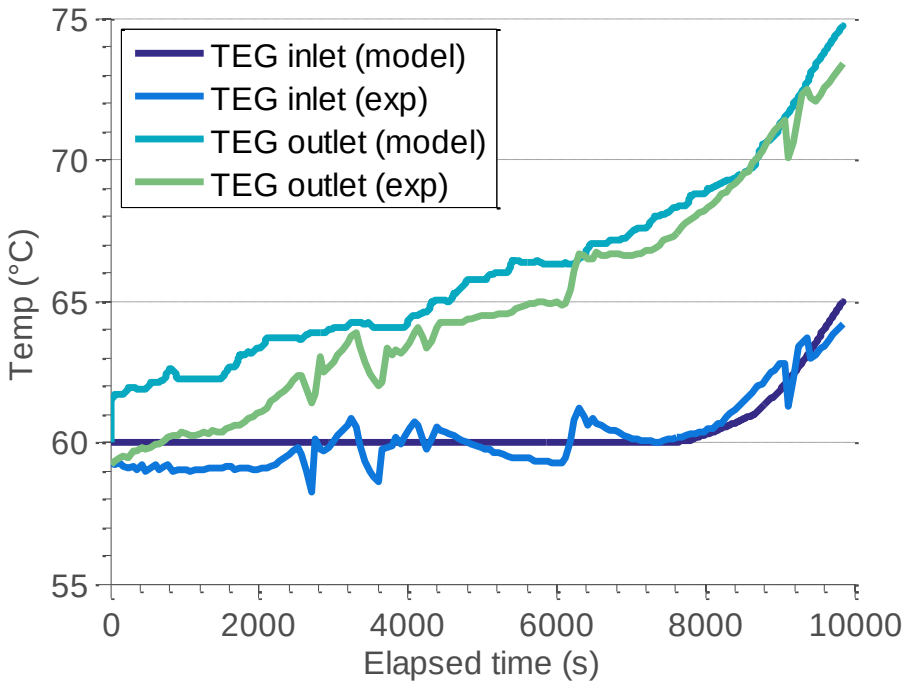

Figure 3.7: Validation of Coolant Loop Numerical Model with Experimental Results.

The energy removed from the hot gas was calculated using $Q_{HHX} = \dot{m}\left(h_{in} - h_{out}\right)$ taking the enthalpies of nitrogen gas at the inlet and outlet of the heat exchanger. REFPROP was used to find fluid properties [22]. It was assumed that the centerline gas temperature was representative of the overall enthalpy. The heater input power was calculated using a similar approach with the heater inlet and outlet temperatures.

The heat input to the coolant (Q_CHX) was calculated for both CHXs and summed to find the total coolant heat input. A constant coolant specific heat using a temperature of 60°C was used, as the fluid temperature was effectively constant. Due primarily to uncertainty in the coolant flow rate, the overall uncertainty for the coolant heat input is roughly 10%. The coolant and exhaust heat transfer values are shown in Figure 3.8.

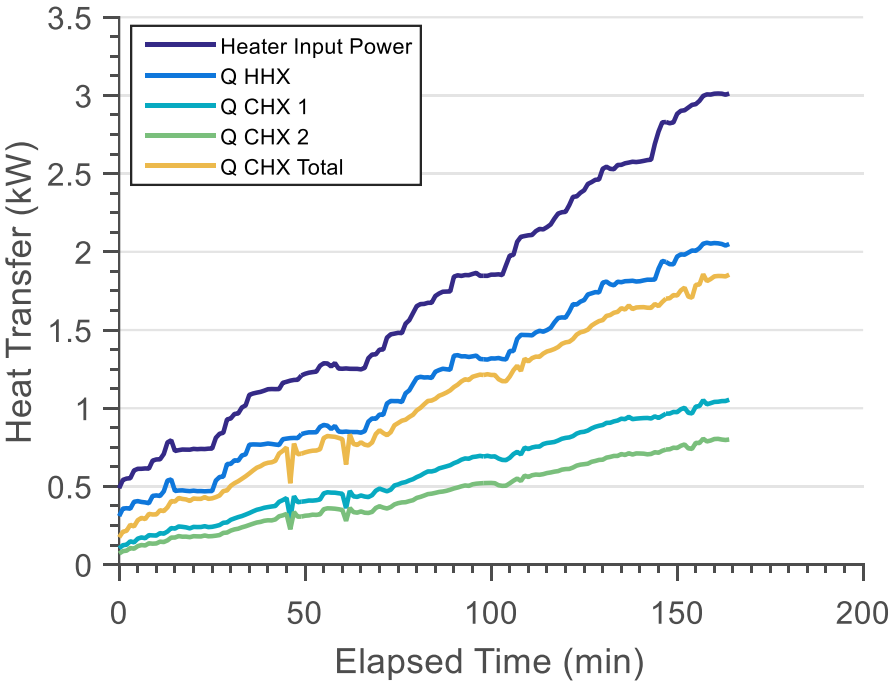

Figure 3.8: TEG Heat-up Energy Balance Accounting.

The difference between the heat removed from the exhaust gas (Q HHX) and the heat entering the cold side heat exchanger (Q CHX Total) was on average 12% +/- 13% of Q_HHX over the course of the test, with high uncertainty carried from the CHX heat input. This value accounts for the sum of stray heat losses, heat converted to electrical power in the TEMs, and thermal storage in the TEG. For these tests the TEMs were kept under open circuit conditions and did not generate power. The stray heat losses accounts for all heat leaving the TEG through radiation and convection from the outer casing, as well as conduction to surrounding components in the exhaust line, and measure the energy bypassing the thermoelectric module stack. The heat and energy transfer processes are shown in Figure 3.9. On the test vehicle these losses are expected to increase as there will be air flow over the case enhancing heat transfer. This will also decrease the casing surface temperature compared to bench testing.

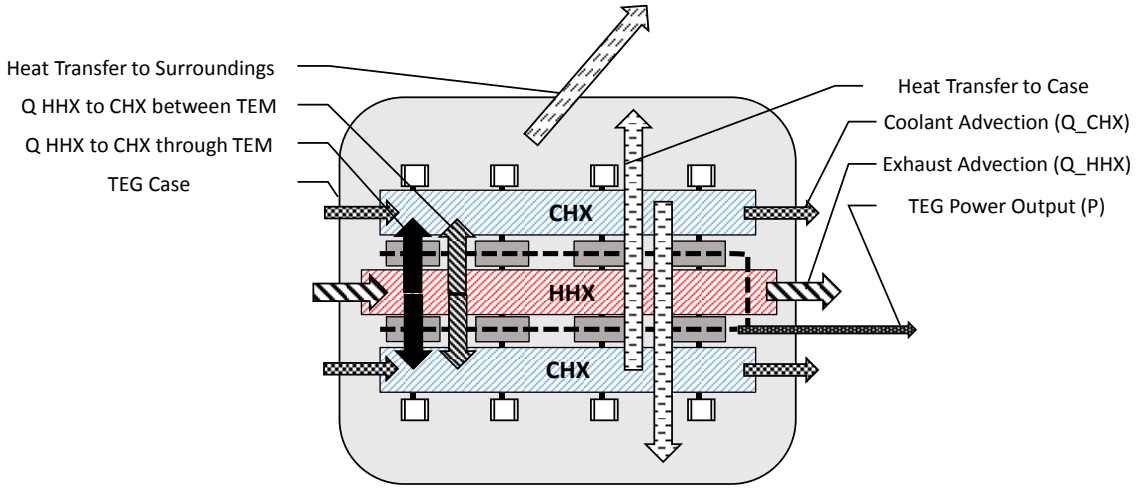

Figure 3.9: Heat and Energy Transfer of TEG System.

By comparing heat transfer at steady state conditions, without drawing power from the modules, the stray heat losses can be estimated. The stray heat losses are composed of heat transfer to the surroundings, and are shown in Figure 3.10. Losses increase linearly with inlet gas temperature, as this increases the temperature between the environment and the TEG. The loss was approximately 6% of the TEG input energy (Q_in) across all temperatures. By improving insulation and minimizing these losses the overall TEG efficiency directly improves, with a potential overall improvement of 6%.

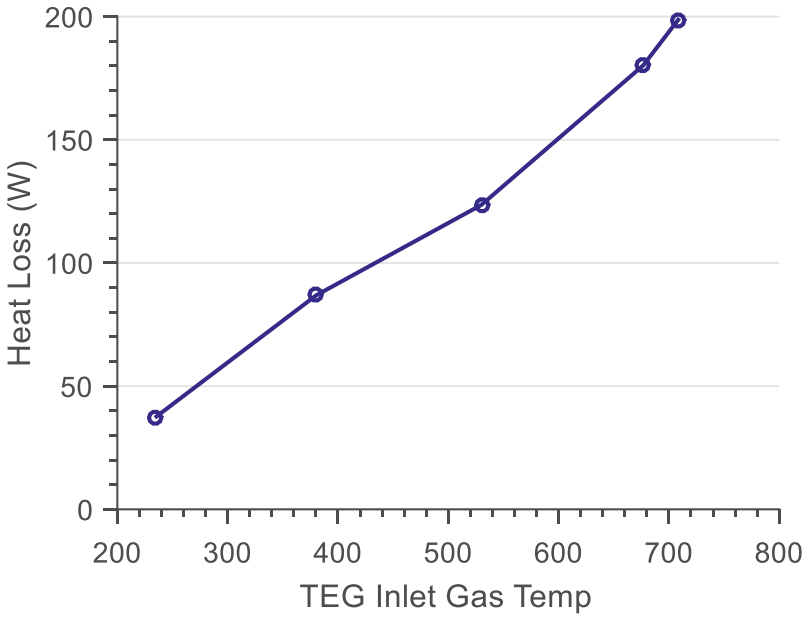

Figure 3.10: Estimated Heat Losses as a function of Inlet Temperature.

An additional loss not captured in these results is heat transfer from the hot to cold side heat exchanger which bypasses the TE legs by travelling through the spaces between TEMs through the insulating blanket, or between legs within a TEM which is

uninsulated space open to the argon environment. These losses will be decreased in future builds through improved insulation.

Average overall heat transfer coefficients were calculated for the hot side heat exchanger at several steady state operating conditions, appearing in Table 3.2. As the working fluid is a gas on the hot side heat exchanger, the heat transfer coefficients are significantly lower than on the coolant side and have a much higher impact on system performance. The overall heat transfer coefficient U (W/m^2-K) was calculated by $U = q/A\left(T_i - T_{hhx,mean}\right)$, where $T_{hhx,mean}$ is average HHX temperature calculated from an arithmetic mean of the HHX skin temperatures at each row, T_i is the gas inlet temperature, and A is the surface area of the heat exchanger. The heat transfer coefficient is found to be nearly independent of gas temperature, while having a strong dependence on the gas flow rate due to increasing Reynold's number.

Table 3.2: Calculated Heat Transfer Coefficients.

Gas Inlet Temp	**Mean HHX Temp**	**Flow Rate**	**Q_HHX**	**U (+/- 0.1)**
°C	°C	g/s	W	W/m^2-K
234.0	99.5	3.30	468	56
380.4	177.5	3.30	853	57
530.1	247.0	3.63	1366	66
676.7	324.3	3.63	1822	67
708.4	322.4	4.01	2040	75

3.2.2 Electrical Performance

A history of the individual module voltages for the heat-up test appears in Figure 3.11. The module voltages are grouped into rows, and though the modules are expected to experience nearly uniform hot side and cold side heat exchangers temperatures within the rows, it is apparent that there is a large variability in individual module performance. A module in the 4th row with unusually low performance was found to have failed mechanically upon teardown and inspection of the prototype TEG, and is not considered in further analysis.

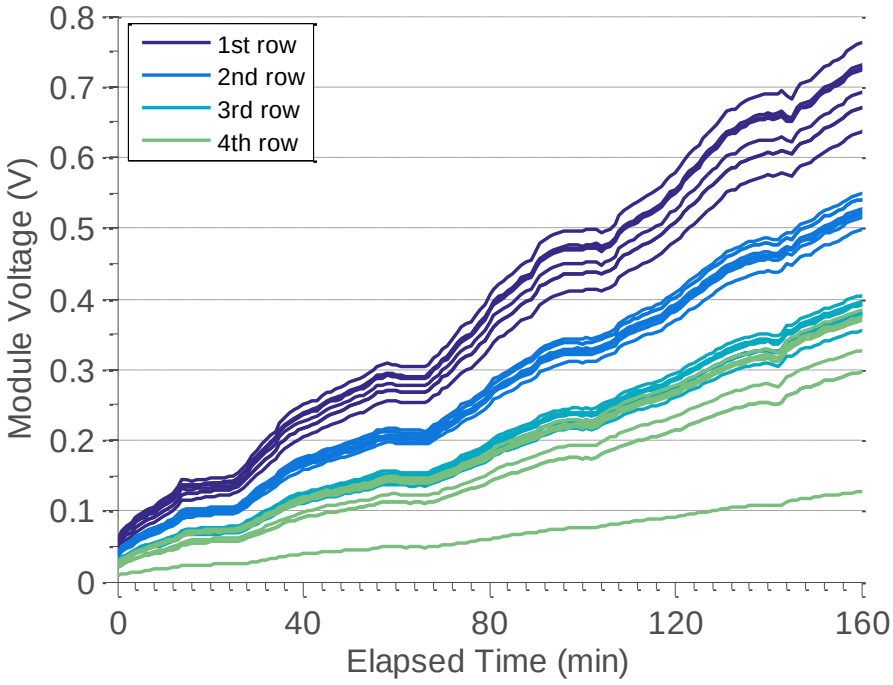

Figure 3.11: TEG Heat-up Individual Module Voltage History.

Potential causes for the variation in TEM performance within rows include individual module degradation or partial failure, non-uniform heat exchanger temperatures, and non-uniform clamping leading to increased contact resistance.

Once steady state conditions at the design point were achieved, a current-voltage characteristic sweep was completed, displayed in Figure 3.12. At this sweep, the generated power was 54 W +/- 3.3 W. If all modules performed as well as the best module in each row, which is a realizable goal, the total power output of the generator would increase by 16% to 63 W at these conditions. A quadratic polynomial was fit to the curve for each row and used to calculate a maximum power point. This procedure was repeated for several different heat exchanger temperatures and used to develop a function for estimating the power output from row open circuit voltage alone.

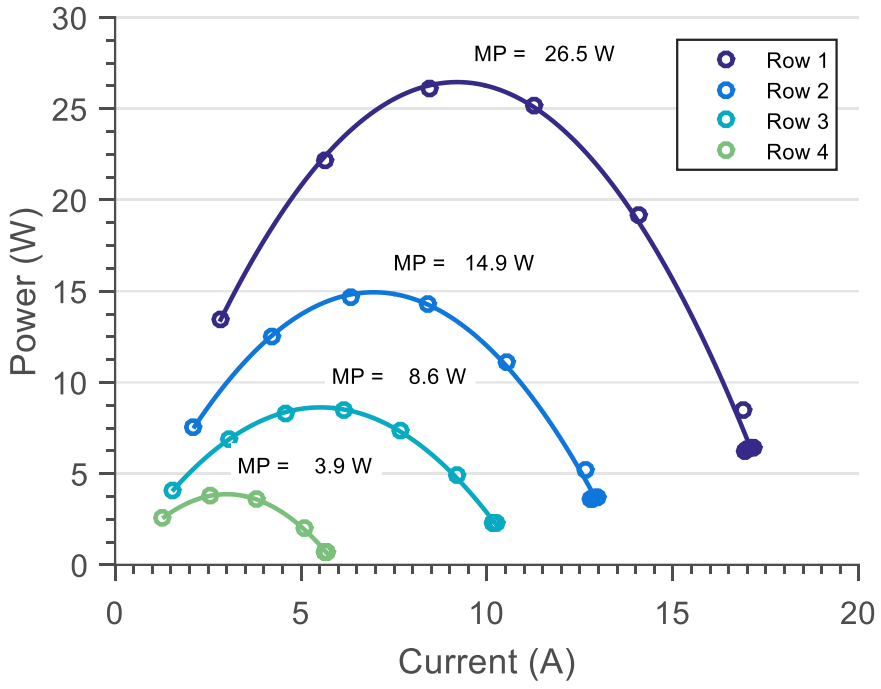

Figure 3.12: Current-Power Curves of 4 TEM Rows at Design Point.

The row open circuit voltages were used to estimate the power output for each of the TEM rows. A simplified estimate of the maximum power point $P = \left(0.5V_{OC}\right)^2 / R_{\text{int}}$ was used, with experimentally calculated values for resistances and experimentally measured open circuit voltages. This was found to give an accurate estimate of the maximum power point. The result is shown in Figure 3.13. The total power output at the design point, and the generator maximum power output, was found to be 54 W, matching IV sweep results.

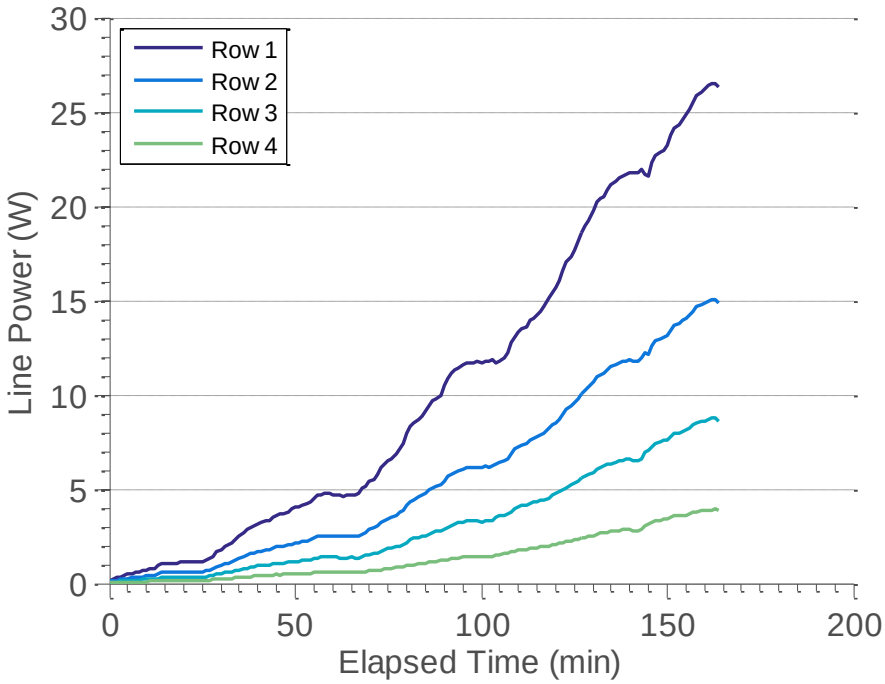

Figure 3.13: TEG Heat-up Row Power Output History.

From these results it can be seen that the 4th row of modules does not contribute significantly to the total system output. It composes approximately 25% of the thermoelectric material, but generates 7% of the total power at the design point.

Defining overall system efficiency as the ratio of output power to heat entering the hot side heat exchanger, efficiency values were calculated vs. the temperature gradient between the hot gas and coolant fluid streams, with results shown in Figure 3.14. The thermal conversion efficiency at the design point was 1.8% +/- 0.17%.

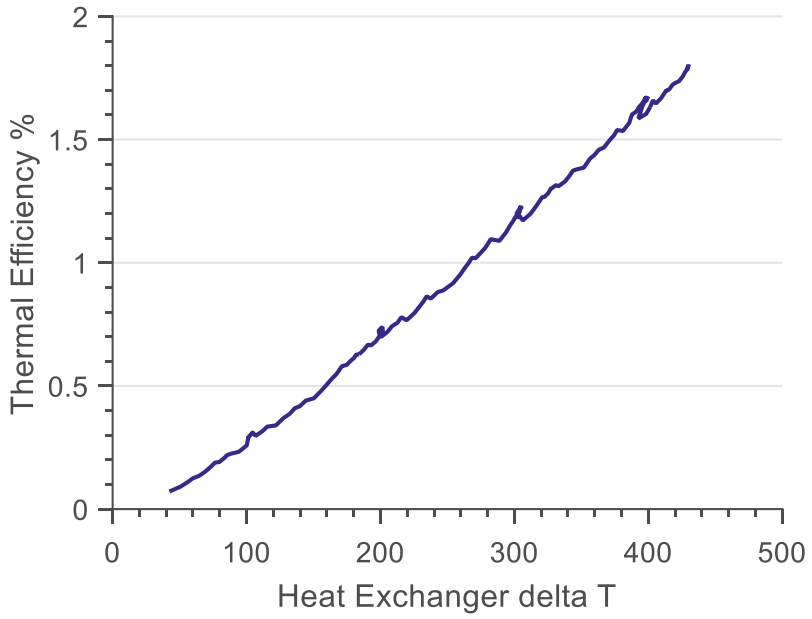

Figure 3.14: TEG Thermal Efficiency vs. Temperature Difference.

The experimental results were found to have close agreement with the numerical model developed by General Motors and Marlow after adjustment of the hot side thermal interface resistance. Thermal resistance results in a reduced temperature difference between the hot and cold side of the TEM modules, and a corresponding reduction in output power. High-resolution imaging of the module to heat exchanger interface completed on teardown of the TEG showed that compliance in the module resulted in non-uniform contact.

3.2.3 Pressure Drop

Cold flow pressure drops were calculated over a range of flow rates, shown in Figure 3.15. Vehicle level modelling showed that the measured back pressure levels have negligible performance impact on the engine. This excess pressure drop budget could allow expansion of the heat exchangers to remove additional heat from the exhaust stream through increased heat exchanger area or denser fin structures.

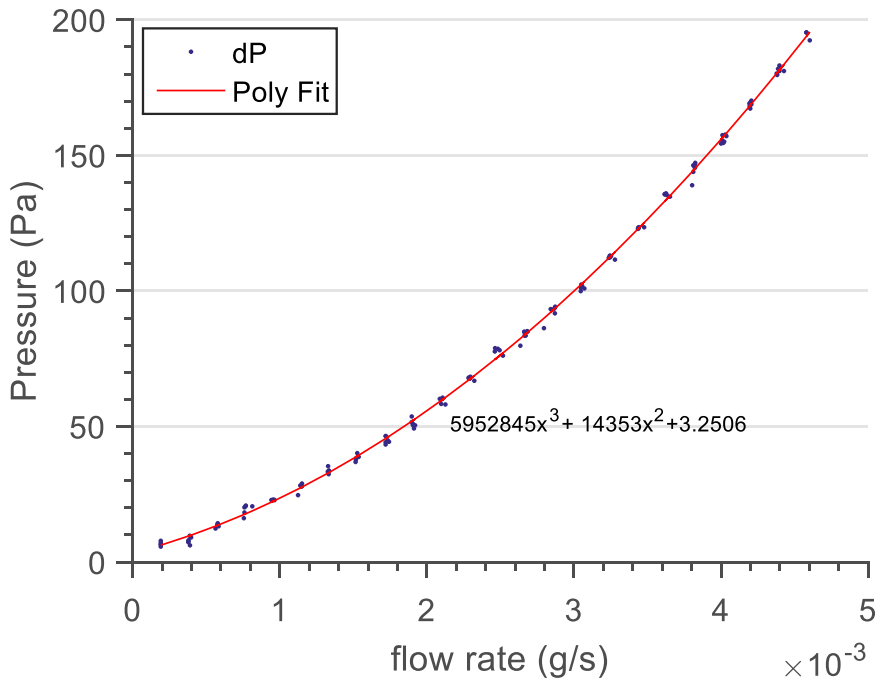

Figure 3.15: Pressure Drop in TEG as a function of Flow Rate.

Using additional data for heated exhaust gas, a correlation for system pressure drop can be constructed for use in vehicle level models.

CHAPTER 4. SUMMARY AND FUTURE WORK

4.1 Overview

The primary goal of this research was to develop a test rig capable of simulating vehicle exhaust gas and coolant in order to perform benchtop TEG performance testing. Using exhaust gas and coolant streams enables full system testing of hot and cold side heat exchangers, TEMs, and thermal interface materials at various scales. Experimental data was used to evaluate TEG performance, verify and correct the analytical model, and justify TEG design decision for the final prototype. Benchtop testing serves as an intermediate step before engine dynamometer and demo vehicle testing.

4.2 Test Bench Summary

The test rig was composed of an exhaust circuit, a coolant loop, power conditioning, and a data acquisition system. The exhaust circuit supplied electrically heated nitrogen up to 760°C with a 6kW stainless steel cased heater featuring an expected life of 5000 hours. An open loop 25 A - 240 V phase angle fired power module was selected to control the heater power, along with a PID temperature controller. Flow control and measurement of the nitrogen gas was accomplished with an Alicat 250 SLMP mass flow controller. The flow controller allowed a maximum flow rate of 4.8 g/s of nitrogen. The

mass flow controller had a settling time of 30ms, which is defined as the length of time necessary for the controller to adjust to a new set point value and settle to the controller's accuracy specifications. This feature was tested in recreating the exhaust mass flow rate profile by sending the controller new set points at a rate of 10Hz using serial communications from custom LabVIEW drivers.

The coolant loop utilized a 50/50 mix of ethylene glycol and distilled water as found in a typical vehicle coolant system. The loop consisted of a 20L reservoir 1100/915 W heated/cooled circulating bath, an 8 psi magnetic drive MARCH 815-BR pump, and an OMEGA FL-9004 piston type variable area flow meter. The coolant loop was modeled and designed in order to maintain constant coolant temperatures over transient cycle testing.

The selected data acquisition system had capacity for 80 analog voltage inputs or 40 differential voltage inputs with 24 digital I/O and 2 analog voltage outputs. It also accepted 32 thermocouple channels. The modular system can be expanded to triple the current channel count for larger scale testing. An electronic load provided the power conditioning for 4 power channels at up to 80 V and 60 A each. A specialized power point tracking algorithm was implemented in LabVIEW to allow efficient power generation tracking of the test unit.

4.3 TEG Performance

Initial testing was completed up to a design point of 710°C nitrogen at a flow rate of 4 g/s, and 60°C coolant at a flow rate of 3.1 LPM. The actual power generated at this condition was 54W with a maximum thermal efficiency of 1.8%. If all the modules in each

row performed as well as the best module in the row, the generator would output 63W. At this design point approximately 6% of the heat energy extracted in the TEG was not collected in the coolant (presumably escaping via the TEG outer casing), and additional insulation could result in up to 6% improvement in the device thermal efficiency.

Imaging of the heat exchanger stack showed bowing in the module. The application of clamping load on the edges of the module resulted in the center of the module separating from the heat exchanger surface, increasing the thermal interface resistance. This must be addressed in future designs to maximize the temperature gradient across the TEMs.

In the first build the space between thermoelectric legs in the module was left uninsulated. This allows a parallel bypass path for heat to flow from the hot to cold side heat exchanger via convection, conduction, and radiation, reducing performance. In a previous study, improving the insulation between thermoelectric legs was found to increase TEM thermal efficiency from 3.2% to 4.5% [8]. For future builds this space will be insulated to improve performance.

4.4 Proposed Future Work

The current project calls for a final TEG prototype to be designed. Based on findings from the reported build, efforts for the final build will focus on decreasing the hot side thermal interface resistance. Additional efficiency improvements will be made by increasing insulation to minimize stray heat losses, creating a sealed inert environment to prevent TEM degradation, and implementing a new compliant topology to minimize

stresses imposed on the TEMs. Overall the final build will serve as a trial for several novel technologies.

Work was initiated on the modelling and experimental analysis of a novel impingement based heat exchanger. Researchers have primarily focused on the use of longitudinal fin based heat exchangers for heat transfer, with thermoelectric modules (TEMs) mounted along the gas flow direction. One drawback to this design is the decreasing temperature and heat flux profiles along the flow direction, which lead to poor performance of trailing TEMs located near the TEG outlet. Additionally, this variation in operating conditions complicates system optimization. Using arrays of hot air jets impinging on TEM surfaces may ensures uniform hot side conditions across the TEG. The heat transfer to the TEMs can be improved with higher surface heat transfer coefficients with enhancements such as pin fins and flow turbulizers in the impingement plenum.

A conceptual TEG, based on jet impingement, has been built. The design allows varying multiple parameters in the design, including the impinging jet diameter and configuration, the spacing between the jet and the target plate, and target plate surface enhancements to improve heat transfer. Further work may establish experimental comparison of impingement and traditional plate flow based heat exchangers for TEG applications.

4.5 Future Outlook

A significant current area of research is the improvement of existing thermoelectric materials and discovery of new materials. Improved figure of merit (ZT)

has a direct impact on TEG performance. Under typical automotive hot side and cold side temperatures of 500°C and 100°C across the generator, a ZT of 5 would result in a thermal conversion efficiency of 25%, similar to that of current internal combustion engines.

The figure of merit can be improved by decreasing the thermal conductivity, increasing the material Seebeck coefficients, or reducing the electrical resistivity. Interesting advances in material science allow accomplishing these contradictory goals, approaching an ideal material which behaves as a 'phonon glass' as well as an 'electron crystal' [13]. Currently available materials have an average ZT of around 1.

It is necessary to maximize the temperature gradient across thermoelectric materials for optimum performance. Modelling has identified thermal interfaces as a critical obstacle due to temperature drop occurring across the interface instead of the thermoelectric material. Some interface resistance is inevitable due to the effects of non-uniform contact and surface roughness, however significant improvements in TEG performance can be achieved through better interface management [36].

One approach for managing thermal interfaces in active development is the use of carbon nanotubes (CNTs). Though difficult to implement, an interface with CNT arrays directly synthesized on both sides has been reported to have a resistance similar to that of a soldered joint [37]. One study found that the use of CNT interfaces compared to no thermal interface material improved TEM output by 60%, though improvements compared to current thermal interface materials (TIMs) will be smaller.

Some challenges to widespread implementation of a CNT thermal interface include high temperatures required for CNT growth, difficulties in direct synthesis on

various surfaces, and limited CNT length in rough surface applications. Additionally, CNTs are sensitive to oxidizing environments at higher temperatures. A possible solution to some of these problems is the use of a thermal interface material (TIM) composed of a metal foil with CNTs synthesized on both sides, which could be inserted between substrates similarly to current TIMs such as graphite foil. This foil would remove the need to customize the CNT synthesis process for different geometries and materials and allow use in numerous applications [37].

The need for improved fuel economy, and globally for sustainable energy usage, is a critical topic which is expected to continue gaining attention. Thermoelectric generators have great potential in waste recovery in numerous applications. Significant strides, including those realized under this collaborative project, are being made in improving generator performance and technology readiness for transportation, commercial, and industrial applications.

LIST OF REFERENCES

LIST OF REFERENCES

[1] "Fuel Economy | National Highway Traffic Safety Administration (NHTSA)." [Online]. Available: http://www.nhtsa.gov/fuel-economy. [Accessed: 19-Feb-2015].

[2] E. I. A. (US), *Monthly Energy Review - January 2015*. Government Printing Office, 2015.

[3] F. Chiara and M. Canova, "A review of energy consumption, management, and recovery in automotive systems, with considerations of future trends," *Proc. Inst. Mech. Eng. Part J. Automob. Eng.*, vol. 227, no. 6, pp. 914–936, Jun. 2013.

[4] J. R. Salvador, J. Y. Cho, Z. Ye, J. E. Moczygemba, A. J. Thompson, J. W. Sharp, J. D. König, R. Maloney, T. Thompson, J. Sakamoto, H. Wang, A. A. Wereszczak, and G. P. Meisner, "Thermal to Electrical Energy Conversion of Skutterudite-Based Thermoelectric Modules," *J. Electron. Mater.*, vol. 42, no. 7, pp. 1389–1399, Jul. 2013.

[5] Committee on the Assessment of Technologies for Improving Light-Duty Vehicle Fuel Economy and National Research Council, *Assessment of Fuel Economy Technologies for Light-Duty Vehicles*. Washington, DC, USA: National Academies Press, 2011.

[6] K. Yazawa and A. Shakouri, "Cost-Efficiency Trade-off and the Design of Thermoelectric Power Generators," *Environ. Sci. Technol.*, vol. 45, no. 17, pp. 7548–7553, Sep. 2011.

[7] S. LeBlanc, S. K. Yee, M. L. Scullin, C. Dames, and K. E. Goodson, "Material and manufacturing cost considerations for thermoelectrics," *Renew. Sustain. Energy Rev.*, vol. 32, pp. 313–327, Apr. 2014.

[8] J. S. Sakamoto, H. Schock, T. Caillat, J.-P. Fleurial, R. Maloney, M. Lyle, T. Ruckle, E. Timm, and L. Zhang, "Skutterudite-Based Thermoelectric Technology for Waste Heat Recovery: Progress Towards a 1 kW Generator," *Sci. Adv. Mater.*, vol. 3, no. 4, pp. 621–632, Aug. 2011.

[9] S. Kumar, S. D. Heister, X. Xu, J. R. Salvador, and G. P. Meisner, “Thermoelectric Generators for Automotive Waste Heat Recovery Systems Part I: Numerical Modeling and Baseline Model Analysis,” *J. Electron. Mater.*, vol. 42, no. 4, pp. 665–674, Apr. 2013.

[10] J.-A. Paik, S. Jones, J.-P. Fleurial, T. Caillat, and J. Sakamoto, “Aerogels as a sublimation suppression layer for thermoelectric power system,” presented at the Materials Research Society 2005 Spring Meeting, Mar-2005.

[11] L. L. Baranowski, G. J. Snyder, and E. S. Toberer, “Concentrated solar thermoelectric generators,” *Energy Environ. Sci.*, vol. 5, no. 10, p. 9055, 2012.

[12] K. Smith and M. Thornton, “Feasibility of thermoelectrics for waste heat recovery in conventional vehicles,” National Renewable Energy Laboratory, 2009.

[13] G. J. Snyder and E. S. Toberer, “Complex thermoelectric materials,” *Nat. Mater.*, vol. 7, Feb. 2008.

[14] J. Yang and F. R. Stabler, “Automotive Applications of Thermoelectric Materials,” *J. Electron. Mater.*, vol. 38, no. 7, pp. 1245–1251, Jul. 2009.

[15] “Space Radioisotope Power Systems - Multi-Mission Radioisotope Thermoelectric Generator.” NASA, Jan-2008.

[16] D. T. Crane and J. W. LaGrandeur, “Progress Report on BSST-Led US Department of Energy Automotive Waste Heat Recovery Program,” *J. Electron. Mater.*, vol. 39, no. 9, pp. 2142–2148, Sep. 2010.

[17] A. Kushch, M. A. Karri, B. T. Helenbrook, and C. J. Richter, “The Effects of an Exhaust Thermoelectric Generator of a GM Sierra Pickup Truck,” in *Proceedings of Diesel Engine Emission Reduction (DEER) conference*, 2004.

[18] G. P. Meisner, “Program Final Report - Develop Thermoelectric Technology for Automotive Waste Heat Recovery,” General Motors Company, Jan. 2012.

[19] K. Yazawa and A. Shakouri, “Optimization of power and efficiency of thermoelectric devices with asymmetric thermal contacts,” *J. Appl. Phys.*, vol. 111, no. 2, p. 024509, 2012.

[20] S. Kumar, S. D. Heister, X. Xu, J. R. Salvador, and G. P. Meisner, “Thermoelectric Generators for Automotive Waste Heat Recovery Systems Part II: Parametric Evaluation and Topological Studies,” *J. Electron. Mater.*, vol. 42, no. 6, pp. 944–955, Jun. 2013.

[21] US. EPA, “EPA US06 or Supplemental Federal Test Procedure (SFTP) | Emission Standards Reference Guide | US EPA.” [Online]. Available: http://www.epa.gov/otaq/standards/light-duty/sc06-sftp.htm. [Accessed: 06-Mar-2015].

[22] E. W. Lemmon, M. L. Huber, and M. O. McLinden, “NIST Standard Reference Database 23: Reference Fluid Thermodynamic and Transport Properties-REFPROP, Version 9.1.” National Institute of Standards and Technology, Standard Reference Data Program, 2013.

[23] “Threaded Inline.” [Online]. Available: http://qa.sylvania.com/en-us/products/air-heaters/process-air-heaters/Pages/threaded-inline.aspx. [Accessed: 17-Mar-2015].

[24] “Watlow | Solid State Controller, DIN-A-MITE C Power Controller.” [Online]. Available: https://www.watlow.com/products/controllers/din-a-mite-c-power-controller.cfm?famid=17. [Accessed: 17-Mar-2015].

[25] “Technical Data for Alicat MC and MCR Mass Flow Controllers.” Alicat Scientific.

[26] “Emerson Process Management - Rosemount 3051 Pressure Transmitter | Rosemount.” [Online]. Available: http://www2.emersonprocess.com/en-us/brands/rosemount/pressure/pressure-transmitters/3051-pressure-transmitters/pages/index.aspx. [Accessed: 05-May-2015].

[27] “Refrigerated Circulating Baths | PolyScience.” [Online]. Available: https://www.polyscience.com/products/circulating-baths/refrigerated-circulators. [Accessed: 05-May-2015].

[28] “March 815-BR Magnetic Drive Pump.” [Online]. Available: http://www.marchpump.com/815-br/. [Accessed: 05-May-2015].

[29] “Easy-view Flowmeters.” [Online]. Available: http://www.omega.com/pptst/FL9000.html. [Accessed: 05-May-2015].

[30] “NI PXI-6255 - National Instruments.” [Online]. Available: http://sine.ni.com/nips/cds/view/p/lang/en/nid/203008. [Accessed: 05-May-2015].

[31] “NI PXIe-4353 - National Instruments.” [Online]. Available: http://sine.ni.com/nips/cds/view/p/lang/en/nid/208291. [Accessed: 05-May-2015].

[32] “Model MDL001, MDL DC Electronic Loads - B&K Precision.” [Online]. Available: http://www.bkprecision.com/products/dc-electronic-loads/MDL001-programmable-dc-electronic-load-mainframe.html. [Accessed: 12-Mar-2015].

[33] R. Faranda and S. Leva, “Energy comparison of MPPT techniques for PV Systems,” *WSEAS Trans. Power Syst.*, vol. 3, no. 6, pp. 446–455, 2008.

[34] R. Rawat and S. S. Chandel, “Review of Maximum-Power-Point Tracking Techniques for Solar-Photovoltaic Systems,” *Energy Technol.*, vol. 1, no. 8, pp. 438–448, Aug. 2013.

[35] “A Photovoltaic MPPT Algorithm for DC Electronic Loads | Test & Measurement content from Electronic Design.” [Online]. Available: http://electronicdesign.com/test-amp-measurement/photovoltaic-mppt-algorithm-dc-electronic-loads. [Accessed: 12-Mar-2015].

[36] K. R. Saviers, S. L. Hodson, T. S. Fisher, J. R. Salvador, and L. S. Kasten, “Carbon Nanotube Arrays for Enhanced Thermal Interfaces to Thermoelectric Modules,” *J. Thermophys. Heat Transf.*, vol. 27, no. 3, pp. 474–481, Jul. 2013.

[37] B. A. Cola, X. Xu, and T. S. Fisher, “Increased real contact in thermal interfaces: A carbon nanotube/foil material,” *Appl. Phys. Lett.*, vol. 90, no. 9, p. 093513, 2007.

APPENDICES

Appendix A Part Numbers

Table A.1: Hardware Part Numbers.

Vendor	**Part**	**Description**
Alicat	MCR-250SLPM-D/GAS:Air,5M,LIN	Mass Flow Controller 0-250 SLPM
Alicat	MCR-2000SLPM-D/GAS:N2,5M,LIN	Mass Controller, 0 - 2000 SLPM
BK Precision	MDL-001	Electronic Load Mainframe
BK Precision	MDL-400	80V/60A/400W Load module
March Pump	815-BR	March 115V Mag Drive Pump
NI	781622-01	NI PXIe-1078, 9-Slot PXI Express Chassis
NI	782450-04	NI PXIe-8135 Core i7-3610QE 2.3 GHz
NI	779547-01	NI PXI-6255
NI	781348-01	NI PXIe-4353 32-Channel TC
NI	782536-01	SCB-68A Connector Block
NI	782403-01	NI TC-4353 Mini TC Terminal Block
Omega	FL-9004	Flowmeter
Osram	F074439	24kW 240V Heater
Polyscience	MX20R-30-A11B	20L Refrigerated Circulator
Rosemount	3051CD1A02A1AH2B2M4Q4	25inh2o Differential Pressure Trans.
Watlow	DC21-24S5-0000	Din-A-Mite SSR
Watlow	DC10-24P5-0000	DIN-A-MITE Power Controller
Watlow	PM8C1FA-AAFAAAA	Temperature Controller

Appendix B Data File Channel List

Table B.1: Data File Channel List.

T_Heater_Out	C	Heater Outlet Temp
T_HHX_In	C	HHX Inlet Temp
T_HHX_Out	C	HHX Outlet Temp
T_HHX_1	C	HHX 1st Row Center
T_HHX_2	C	HHX 2nd Row Center
T_HHX_3	C	HHX 3rd Row Center
T_HHX_4	C	Interior Case Temp
T_HHX_5	C	HHX 4th Row Center
T_HHX_6	C	PCB Temp
T_HHX_7	C	Coolant Outlet Line Temp
T_HHX_8	C	HHX Temp 8 - Unwired
T_CHX1_In	C	CHX1 Coolant Inlet Temp
T_CHX1_Out	C	CHX1 Coolant Outlet Temp
T_CHX2_In	C	CHX2 Coolant Inlet Temp
T_CHX2_Out	C	CHX2 Coolant Outlet Temp
V_01	volts	Voltage Sense TEM 1
V_02	volts	Voltage Sense TEM 2
V_03	volts	Voltage Sense TEM 3
V_04	volts	Voltage Sense TEM 4
V_05	volts	Voltage Sense TEM 5
V_06	volts	Voltage Sense TEM 6
V_07_08	volts	Voltage Sense TEM 7 + 8
V_09	volts	Voltage Sense TEM 9
V_10	volts	Voltage Sense TEM 10
V_11_12	volts	Voltage Sense TEM 11 + 12
V_13	volts	Voltage Sense TEM 13
V_14	volts	Voltage Sense TEM 14
V_15	volts	Voltage Sense TEM 15
V_16	volts	Voltage Sense TEM 16
V_17	volts	Voltage Sense TEM 17
V_18	volts	Voltage Sense TEM 18
V_19	volts	Voltage Sense TEM 19
V_20	volts	Voltage Sense TEM 20
V_21	volts	Voltage Sense TEM 21

Table B.1: Continued.

V_22	volts	Voltage Sense TEM 22
V_23_24	volts	Voltage Sense TEM 23+24
V_25	volts	Voltage Sense TEM 25
V_26	volts	Voltage Sense TEM 26
V_27_28	volts	Voltage Sense TEM 27 + 28
V_29	volts	Voltage Sense TEM 29
V_30	volts	Voltage Sense TEM 30
V_31	volts	Voltage Sense TEM 31
V_32	volts	Voltage Sense TEM 32
P_heater	W	Heater Power
delta_P	Pa	TEG Pressure Drop
V_Row1	volts	TEM Row 1 Voltage
V_Row2	volts	TEM Row 2 Voltage
V_Row3	volts	TEM Row 3 Voltage
V_Row4	volts	TEM Row 4 Voltage
I_Row1	volts	TEM Row 1 Current
I_Row2	amps	TEM Row 2 Current
I_Row3	amps	TEM Row 3 Current
I_Row4	amps	TEM Row 4 Current
Gas Flowrate	amps	Gas Flowrate
Gas Setpoint	SLPM	Gas Controller Setpoint
T_inlet	SLPM	Mass Flow Controller Inlet Temp
P_inlet	C	Mass Flow Controller Outlet Pressure
Coolant Flowrate	PSI	Coolant Flow Rate (Manual Input)
Time	LPM	Timestamp